dc_1631_19

Numerical Investigations of Turbulent Structures in Fluids

Doctoral thesis

submitted to the Doctoral Committee of the Hungarian Academy of Sciences

Gábor Janiga, Ph.D.

2019

dc_1631_19

Acknowledgements

I wish to record my sincere thanks to Professor Tibor Czibere for his creative influence on my professional activities and for his direct or indirect contribution to this work.

I acknowledge the support of Prof. Dominique Thévenin which provided an environment in which all the ideas were developed.

I am also grateful to the numerous colleagues and coauthors in Miskolc and in Magdeburg over the years.

Special appreciation goes to my family, especially to my wife and my daughter, for providing the necessary atmosphere of understanding and support during the untold amount of hours at home required for preparing this thesis.

dc_1631_19

Acronyms

BPF	Blade passage frequency
CFD	Computational Fluid Dynamics
CFL	Courant-Friedrichs-Lewy (number)
DEISA	Distributed European Infrastructure for Supercomputing Applications
DNS	Direct Numerical Simulation
FDA	Food and Drug Administration, USA
HPC	High Performance Computing
LDV	Laser-Doppler Velocimetry
LES	Large Eddy Simulation
MI	Macro-instability
MRI	Magnetic Resonance Imaging
NSCBC	Navier-Stokes Characteristic Boundary Conditions
NITA	Non-Iterative Time Advancement
PC-MRI	Phase-contrast Magnetic Resonance Imaging
PIV	Particle Image Velocimetry
POD	Proper Orthogonal Decomposition
PTV	Particle Tracking Velocimetry
RANS	Reynolds-averaged Navier-Stokes
SBES	Stress-Blended Eddy Simulation
SPOD	Snapshot Proper Orthogonal Decomposition
SVD	Singular Value Decomposition
URANS	Unsteady Reynolds-averaged Navier-Stokes

dc_1631_19

Contents

Chapter 1

Introduction

Fluid flow problems play an important role in many practical applications, for example for energy generation, chemical engineering, biomedical flows or environmental problems. The fluid elements show a fluctuating and chaotic motion in the majority of these applications. The understanding and modeling of these so-called turbulent flows are much more challenging than laminar flows.

1.1 Introduction to Computational Fluid Dynamics

Fluid flow problems can be described by partial differential equations (see later in Chapter 2). Their analytical solution in a closed form exists only in special cases. These analytical solutions are particularly important to understand fluid flow phenomena, but they cannot be directly applied for solving real engineering problems.

Because of the enormous increase of computing capacity in the last decades the numerical solutions of partial differential equations are becoming more and more attractive. Parallel to the evolution of the computers, more and more advanced numerical methods have been developed. The immense progress in both computing hardware and numerical techniques led subsequently to the birth of the field which is today known as *Computational Fluid Dynamics*

(or shortly CFD). In the frame of CFD the governing equations are solved numerically.

The numerical solution based on a discretization method translates the differential equations into a system of algebraic equation. This algebraic equation system can then be solved on computers. During the discretization the considered domain is divided into small parts, i.e., discrete points or discrete volumes. The variables are calculated only at these discrete locations and are only defined on the numerical grid. It is the discrete representation of the considered continuous problem, obtained by dividing the computational domain into a finite number of small parts (control volumes or elements). If unsteady effects are important, time is also considered as discrete time points. The accuracy of the obtained numerical solution is influenced by the characteristics of the applied discretization.

Three types of systematic errors can be distinguished, as described in [24]:

- Modeling errors: the difference between the actual flow and the exact solution of the mathematical model (wrong or incomplete physical models).
- Discretization errors: the difference between the exact solution of the conservation equations and the exact solution of the algebraic system of equations obtained by discretizing these equations.
- Iteration errors: the difference between the iterative and the exact solutions of the algebraic equation systems.

In addition, human errors should be mentioned, when applying inappropriate boundary conditions or wrong model settings.

The Navier-Stokes equations fully govern the flow of a viscous fluid. The same equation system can predict completely different flow configurations. Due to different boundary conditions, the same equation system dictates different solutions. Accurate and proper boundary conditions are especially important for CFD!

Three main solution approaches can be distinguished for solving numerical fluid flow problems. These are:

- finite differences [7, 63],
- finite volumes [24, 82],
- finite elements [56].

These techniques are partly similar, but also have their special features. All of these methods have advantages and disadvantages. Other dedicated techniques exist for special applications. In what follows, the finite volume method is applied in Chapter 3 and in Chapter 4. The finite difference method is con-

sidered in Chapter 5. These methods are not further discussed here. Excellent overviews are available in the already cited textbooks.

1.2 Modeling of Turbulent Flows

Depending on the value of a key non-dimensional number, the Reynolds number, every flow can be predicted to be laminar or turbulent. Turbulent flows can be found in most practical applications but are much more complex than laminar flows, because of their chaotic nature.

The increase in computing power and the development of numerical algorithms in recent decades has made CFD a widely used approach for complex engineering configurations. Nonetheless, progress in the modeling of the turbulent flows has not been that rapid.

In a high number of the engineering applications, the numerical solution still relies on the Reynolds-averaged Navier-Stokes (RANS) equations. In the RANS approach, each flow variable is decomposed into a deterministic time-average and a stochastic (turbulent) fluctuation. The purpose of RANS is the correct prediction of the time-averaged variables. Due to the averaging process underlying RANS, unknown correlation terms appear in the governing equations. These are the elements of the so-called Reynolds-stress tensor. The resulting number of unknowns is larger than the available number of equations, leading to the so-called closure problem [66]: in order to solve the system of equations a turbulence model is required. Widely used models are the $k-\varepsilon$ and $k-\omega$ engineering turbulence models, as well as further variants derived from them [84]. These models still contain various model parameters, deduced from simple canonical flows.

These equations have been the subject of numerous studies over the last 50 years, but none of the RANS models have been determined to be superior for all types of flows without the use of some fine-tuning of the model parameters or constants (see, e.g., [78]). This could be due to the significant influence of the boundary conditions on the large energy-carrying turbulent eddies. Therefore, considering the dynamics of these eddies, the development of a universal RANS model might not be possible at all [59].

The direct numerical simulation (DNS) of the Navier-Stokes equations does not rely on any turbulence model. In this approach, the discretized governing equations are directly solved on a very fine computational grid with a large number of small time steps (see, e.g., [5]). All physically important scales are resolved – up to the so-called Kolmogorov scales – on the employed grid both

in space and time. This very interesting method is still computationally prohibitive even for intermediate Reynolds numbers. In practice, this still remains challenging for everyday engineering problems, and will continue to be so even in the next decades despite of the rapidly increasing power of supercomputers.

The limitations of RANS and the unmanageable computational efforts of DNS have led to the rapid development of large eddy simulations (LES), as a compromise between both [30, 71]. The LES approach spatially filters only the small-scale turbulent structures, which have less effect on the overall energy budget. They can furthermore be considered as isotropic, and are therefore easier to model. At the same time, the large scale – anisotropic – structures are directly resolved on the employed grid, as in DNS. The spatial filtering again introduces unknown terms in the governing equations, the subgrid tensor. Since there are more unknown terms than the available number of equations, modeling is again required at the small scales, called the subgrid-scale (SGS) model.

Large eddy simulations can be considered as an intermediate approach between DNS and the solution of the RANS equations. In the past 15-20 years, LES has emerged and developed into a mature state in the study of turbulent flows including various mechanical, chemical and process engineering applications.

Generally speaking, LES simulations require a higher computational mesh resolution and shorter time steps than an unsteady RANS computation. Nevertheless, the computational efforts are far lower than those required for DNS. The continuous increase in computer resources makes LES more and more accessible for various engineering problems. When directly resolving at least 80% of the total amount of kinetic energy – a typical target for high-quality LES simulations [66] –, the obtained information concerning turbulent flows should be far more than that accessible by any RANS approach.

1.3 Outline

In this work, several turbulent flow problems are considered for various engineering applications involving CFD. All these problems result in a considerable computational effort, therefore parallel computations are absolutely necessary.

This work is structured as follows. The governing equations are discussed in Chapter 2.

The flow prediction in a biomedical device is examined first in Chapter 3. Although CFD is now extensively used for a broad range of industrial applica-

tions, but most medical scientists still do not consider CFD as a mature tool for biomedical flow simulations. In order to check this point, the FDA (Food and Drug Administration, USA) decided to propose several benchmark cases in order to study the validity and accuracy of CFD predictions for exemplary biomedical applications. A blood nozzle benchmark case is investigated in this work [79] considering $\mathrm{Re} = 6\,500$, since it is challenging from the point of view of the flow state. After the characterization of the different flow regimes, the performance of a hybrid simulation is investigated in order to to reduce the computational costs.

In the second application example the time-dependent three-dimensional hydrodynamics in a stirred tank reactor is characterized by using numerical simulations (Chapter 4). The rotating propellers produce a complex, unsteady, three-dimensional turbulent flow field. This results in efficient mixing and is therefore widely used in various process and chemical engineering applications. The time-dependent turbulent single-phase flow is computed using large eddy simulation, relying on the sliding mesh approach. The dominant coherent flow structures are characterized in the entire three-dimensional computational domain by using the 3D proper orthogonal decomposition (POD) technique. Furthermore, the macro-instability (MI) is examined by monitoring the fluid velocity in more than one million computational cells.

Applications involving turbulent flows with chemical reactions play an essential role in our daily life. All our transportation systems and the overwhelming majority of our energy supply rely directly or indirectly on the combustion of fossil fuels. In order to improve the efficiency of such systems and to develop new approaches and configurations, numerical simulations play an increasing role in research and industry. They provide a cost-efficient complement to experimental testing and prototypes. But, of course, they are only useful if they can accurately reproduce the real physical processes controlling practical configurations. Chapter 5 is devoted to the direct numerical simulation of turbulent premixed methane-air flames.

The new scientific results are summarized in Chapter 6.

dc_1631_19

Chapter 2

Governing Equations

2.1 Governing Equations of Reactive Flows

During the last decades, numerical combustion modeling has become a natural complement to experiments, in particular to investigate in detail complex physical processes in realistic setups.

For a gas mixture the mass conservation and the Navier-Stokes equations can be written as:

$$\frac{\partial \rho}{\partial t} + \frac{\partial(\rho u_j)}{\partial x_j} = 0 \tag{2.1}$$

$$\frac{\partial(\rho u_i)}{\partial t} + \frac{\partial(\rho u_j u_i)}{\partial x_j} = -\frac{\partial p}{\partial x_i} + \frac{\partial \tau_{ij}}{\partial x_j} \ , \tag{2.2}$$

where ρ denotes mixture density, u_j the components of the hydrodynamic velocity, p the pressure, and τ_{ij} the stress tensor.

The additional balance equations expressing the conservation of chemical species and energy assuming ideal gas are given as:

$$\frac{\partial(\rho Y_k)}{\partial t} + \frac{\partial(\rho u_j Y_k)}{\partial x_j} = -\frac{\partial(\rho Y_k V_{kj})}{\partial x_j} + \dot{\omega}_k; \quad k = 1, 2, ..., N_{sp} \tag{2.3}$$

$$\frac{\partial(\rho e_t)}{\partial t} + \frac{\partial[(\rho e_t + p)u_j]}{\partial x_j} = -\frac{\partial q_j}{\partial x_j} + \frac{\partial(\tau_{ij} u_i)}{\partial x_i} \tag{2.4}$$

$$\frac{p}{\rho} = \frac{R}{\overline{W}} T \ , \tag{2.5}$$

where N_{sp} the total number of chemical species, V_{kj} the component of the diffusion velocity of species k in the direction j, $\dot{\omega}_k$ the chemical production rate of species k and q_j the j^{th}-component of the heat flux vector.

The stress tensor τ assuming a Newtonian-fluid:

$$\tau_{ij} = \mu \left[\frac{\partial u_i}{\partial x_j} + \frac{\partial u_j}{\partial x_i} \right] + \left(-\frac{2}{3}\mu \right) \frac{\partial u_k}{\partial x_k} \delta_{ij} \tag{2.6}$$

with δ the Kronecker symbol (i.e., $\delta_{ij} = 1$ if $i = j$ and $\delta_{ij} = 0$ otherwise) and μ the dynamic (or shear) viscosity.

2.2 Large Eddy Simulation of Non-reacting Flows

In the large eddy simulation (LES) approach the flow variables are decomposed using a filter to separate resolved scale – responsible for the large-scale inhomogeneous motions –, from subgrid scale – representing the small-scale, supposedly homogenous structures. The flow variables obtained in a large eddy simulation after the spatial filtering are denoted with the symbol $\bar{}$. For an incompressible flow, as considered in Chapter 3 and Chapter 4, the filtered continuity equation reads:

$$\frac{\partial \bar{u}_i}{\partial x_i} = 0 \tag{2.7}$$

and the filtered momentum equation for a Newtonian fluid can be written as:

$$\frac{\partial}{\partial t} \left(\rho \bar{u}_i \right) + \frac{\partial}{\partial x_j} \left(\rho \bar{u}_i \bar{u}_j \right) = -\frac{\partial \bar{p}}{\partial x_i} + \mu \frac{\partial}{\partial x_j} \left(\frac{\partial \bar{u}_i}{\partial x_j} + \frac{\partial \bar{u}_j}{\partial x_i} \right) - \frac{\partial \tau_{ij}}{\partial x_j} \ . \tag{2.8}$$

The fluid is considered here as isothermal, incompressible, and having Newtonian properties. The subgrid tensor τ_{ij} is often expressed as the sum of the Leonard tensor, cross-stress tensor and Reynolds subgrid tensor [71]:

$$\tau_{ij} = \rho \overline{u_i u_j} - \rho \bar{u}_i \bar{u}_j = L_{ij} + C_{ij} + R_{ij} \ . \tag{2.9}$$

Most of the eddy viscosity models are given in the form:

$$\tau_{ij} - \frac{1}{3} \tau_{kk} \delta_{ij} = -2 \mu_t \bar{S}_{ij} \ , \tag{2.10}$$

where δ_{ij} is the Kronecker symbol (which is 1 if $i = j$, otherwise 0), μ_t is the – scalar – subgrid-scale turbulent viscosity, and the rate-of-strain tensor $\bar{S}_{ij}$ for the resolved scale is given by:

$$\bar{S}_{ij} = \frac{1}{2}\left(\frac{\partial \bar{u}_i}{\partial x_j} + \frac{\partial \bar{u}_j}{\partial x_i}\right) . \tag{2.11}$$

CFD codes offer various subgrid-scale models: the Smagorinsky [74] and the dynamic Smagorinsky-Lilly [54] models amongst others. The former is applied in the present work. The eddy viscosity in the Smagorinsky model is represented as:

$$\mu_t = \rho L_s^2 \left|\bar{S}\right| \text{ and } \left|\bar{S}\right| = \sqrt{2\bar{S}_{ij}\bar{S}_{ij}} . \tag{2.12}$$

The original Smagorinsky model [74] does not consider zero eddy-viscosity for laminar shear flows. For wall-bounded flows, a damping factor depending on the wall-normal distance is applied in ANSYS Fluent. Hence, the mixing length L_s for subgrid scales in ANSYS Fluent is defined by [8]:

$$L_s = \min\left(\kappa\, d\, , C_s\, V^{1/3}\right) , \tag{2.13}$$

where κ is the von Kármán constant, d is the distance to the closest wall, V is the volume of the local grid element, and C_s is the non-dimensional coefficient called the Smagorinsky constant. The Smagorinsky constant $C_s = 0.1$ – the default value in ANSYS Fluent [8] – is retained for the presented cases in Chapter 3 and Chapter 4.

2.3 Reactive Flows

The basic notation commonly used in numerical combustion is introduced in this section considering a methane-air mixture.

The global reaction mechanism for a methane-air mixture is written as:

$$\mathrm{CH_4} + 2\,(\mathrm{O_2} + 3.76\,\mathrm{N_2}) \longrightarrow \mathrm{CO_2} + 2\,\mathrm{H_2O} + 7.52\,\mathrm{N_2} \tag{2.14}$$

The air is typically given as 1 mole of oxygen complemented by 3.76 moles of nitrogen. This single step reaction is composed of many elementary chemical reactions. The chemical mechanism of Smooke with 25 elementary reactions (Appendix A) is applied in Chapter 5 investigating methane-air flames.

In order to quantify the ratio of the fuel and the oxidizer in a methane-air mixture, the notation of mixing ratio α can be introduced. This mixing ratio is defined as the ratio of the mass flow rate of the fuel (methane) and the mass flow rate of oxidant (air):

$$\alpha = \frac{\dot{m}_{\mathrm{CH_4}}}{\dot{m}_{\mathrm{air}}} \quad . \tag{2.15}$$

The reaction is considered stoichiometric when the two flow rates are balanced, i.e., exactly the amount of oxidizer and fuel are used to completely burn. The corresponding mixing ratio α_s – with the help of the molecular weights W – is:

$$\alpha_s = \frac{W_{\mathrm{CH_4}}}{2\left(W_{\mathrm{O_2}} + 3.76\, W_{\mathrm{N_2}}\right)} \quad . \tag{2.16}$$

The equivalence ratio ϕ of a methane-air mixture is defined as the ratio of mixing ratio α and α_s:

$$\phi = \frac{\alpha}{\alpha_s} \quad . \tag{2.17}$$

A stoichiometric mixture has a value of $\phi = 1$. A mixture containing an excess of methane is called rich flame ($\phi > 1$), or it is lean if it contains an excess of air ($\phi < 1$).

2.4 Description of the Gas Mixture

In the flame zone a large number of chemical species are involved in a complex process including many elementary reactions and possibly heat release. Some chemical species do not represent a large fraction of the whole mixture, but they may play an essential role in the reaction process as intermediate radicals [36].

The gas mixture is described using a predefined set of chemical species. The complexity of this representation depends on the desired accuracy. The total number of chemical species taken into account in the reactive mixture is denoted N_{sp}.

The thermodynamic state of the gas mixture can be described by its composition, temperature and pressure. The composition of the mixture can be given by all the mass fractions of chemical species. Each species k is associated to its mass fraction Y_k, which represents the mass of species k per unit mass of the mixture:

$$Y_k = \frac{\rho_k}{\rho} \quad . \tag{2.18}$$

The last species is supposed to be the dilutant (nitrogen in our applications) and its mass fraction can be deduced from the other mass fractions:

$$\sum_{k=1}^{N_{sp}} Y_k = 1 \quad \text{yields} \quad Y_{N_2} = 1 - \sum_{k=1}^{N_{sp}-1} Y_k \ . \tag{2.19}$$

As a consequence, $N_{sp} - 1$ transport equations must be solved to compute the composition of the reactive mixture. An additional equation will also be written for the energy balance. It is more usual to consider the specific enthalpy than the internal energy as the former is conserved through chemical processes at constant pressure and with adiabatic boundaries.

The mole fraction X_k of species k is defined by the ratio between the numbers of n_k moles of the given species k and the total number of moles n_t of the mixture:

$$X_k = \frac{n_k}{n_t} \ . \tag{2.20}$$

The average molar mass mixture of W is defined as follows:

$$W = \sum_{k=1}^{N_{sp}} X_k \, W_k \ , \tag{2.21}$$

where W_k is the molar mass of species k.

The mass fractions and mole fractions are related by the following equality:

$$Y_k = \frac{W_k}{W} X_k \ . \tag{2.22}$$

The average molecular weight of the mixture according mass fractions can also be expressed:

$$W = \left(\sum_{k=1}^{N_{sp}} \frac{Y_k}{W_k} \right)^{-1} \ . \tag{2.23}$$

The enthalpy h of the mixture is given with the help of the species enthalpies, themselves being functions of temperature, specific heats at constant pressure c_{pk} and of the standard formation enthalpies h_k^0 at standard temperature T_0:

$$h = \sum_{k=1}^{N_{sp}} Y_k h_k \tag{2.24}$$

and for each species:

$$h_k(T) = h_k^0(T_0) + \int_{T_0}^{T} c_{pk}(T')\,\mathrm{d}T' \quad . \tag{2.25}$$

The enthalpy of mixture can also be written:

$$h = h^0(T_0) + \int_{T_0}^{T} c_p(T')\mathrm{d}T' \ , \tag{2.26}$$

where h^0 is the enthalpy of mixture at the reference temperature:

$$h^0(T_0) = \sum_{k=1}^{N_{sp}} Y_k h_k^0(T_0) \tag{2.27}$$

and c_p is the average specific heat of the mixture given by:

$$c_p = \sum_{k=1}^{N_{sp}} Y_k c_{pk} \quad . \tag{2.28}$$

2.5 Chemical Reactions

The detailed chemistry method is applied to describe the reaction processes in Chapter 5, therefore, it is discussed next.

The overall chemical mechanism is modeled by I elementary reactions involving maximum 3 reactants and 3 products. Each elementary reaction (using index i) can be written as:

$$\sum_{k=1}^{N_{sp}} \nu'_{ki} \mathcal{X}_k \rightleftharpoons \sum_{k=1}^{N_{sp}} \nu''_{ki} \mathcal{X}_k \tag{2.29}$$

with ν'_{ki} and ν''_{ki} as stoichiometric coefficients (0 for most species or 1, maximum 2) The molar production rate of one species k per unit volume is given as:

$$\dot{\omega}_k = \sum_{i=1}^{I} (\nu''_{ki} - \nu'_{ki}) \left\{ k_{f_i} \prod_{k=1}^{N_{sp}} [\mathcal{X}_k]^{\nu'_{ki}} - k_{r_i} \prod_{k=1}^{N_{sp}} [\mathcal{X}_k]^{\nu''_{ki}} \right\} \ , \tag{2.30}$$

where $[\mathcal{X}_k]$ is the concentration of species k and the forward and backward rates of progress of each reaction (k_{f_i} and k_{r_i}) are related to each other via the reaction equilibrium constant. These rates are modeled by the Arrhenius law:

$$k_{f_i} = A_i T^{\beta_i} \exp\left(\frac{-E_i}{R\,T}\right) \tag{2.31}$$

and

$$k_{r_i} = \frac{k_{f_i}}{\mathrm{Ke}_i} \quad . \tag{2.32}$$

The equilibrium constant Ke_i can be determined from the standard enthalpy and entropy as a function of temperature.

For all reactive flow computations presented in Chapter 5, the complete set of chemical species and elementary reactions, with their Arrhenius coefficients A_i, β_i and E_i, is taken from [12, 75] (Appendix A).

2.6 Proper Orthogonal Decomposition (POD)

Proper orthogonal decomposition (POD) is a promising method for the analysis and synthesis of experimental or computational data. It serves also a basis for the determination of low-dimensional dynamic models of complex systems, see, e.g., [39]. Considering only a few modes, a large amount of kinetic energy can be captured. It allows for reduced order models of a complex spatial-temporal system to be built. Conveniently, POD analysis is a linear procedure, nonetheless, it can be applied for non-linear systems without assuming linearity.

The classical proper orthogonal decomposition introduced by Lumley [58] considers the spatial correlation of the flow field realization. The solution of the system involves a singular value decomposition (SVD), therefore, this method is also referred as the SVD method. In practice, this method is limited to moderate spatial resolution – especially for two-dimensional experimental data – because of the computational expenses.

The alternative POD realization, introduced by Sirovich [73], takes the temporal correlation into consideration. This approach is often referred to as snapshot POD or briefly SPOD. The SPOD method is computationally more beneficial for a larger spatial resolution.

Both of these methods have been extensively analyzed and compared for complex flows in two-dimensional planes – involving both two and three ve-

locity components – in [9]. The purpose of the current work is to investigate complex three-dimensional flows, therefore, the two-dimensional SPOD implementation applied in [9] is extended for three-dimensional domains.

The POD technique offers a broad range of applications in fluid dynamics. It can be used to compare different time-varying three-dimensional flow data [45]. The POD analysis supports the feature-based visualization, where the most energetic flow features can be extracted [44]. According to Lumley [58] the flow representation having a largest projection onto the flow defines the coherent flow structures. A given coherent structure is an eigenmode of the two-point correlation matrix of the snapshot database.

The computational details of both the SVD and the SPOD methods are detailed in [9]. Here, only a the SPOD method is briefly summarized.

2.6.1 Snapshot POD Method

The developed method was inspired by Snapshot Proper Orthogonal Decomposition (SPOD, see [73]), but for a completely different objective. The fundamental idea behind POD is to decompose each signal $\mathbf{u}(\mathbf{x}, t_k)$ into orthogonal deterministic functions ϕ (POD spatial modes) and time-dependent coefficients a_k (POD temporal coefficients):

$$\mathbf{u}(\mathbf{x}, t_k) = \sum_{l=1}^{\infty} a_k^l \, \phi^l(\mathbf{x}) \; . \tag{2.33}$$

Here, superscript l and subscript k refer to the mode number and index of corresponding snapshot (or time step), respectively. The function ϕ denotes the eigenfunction of the Fredholm integral equation

$$\int_{\mathbf{X}} \mathbf{R}(\mathbf{x}, \mathbf{x}') \cdot \phi(\mathbf{x}') \, \mathrm{d}\mathbf{x}' = \lambda \phi(\mathbf{x}) \; . \tag{2.34}$$

The kernel of this eigenvalue problem is the two-point spatial correlation function

$$\mathbf{R}(\mathbf{x}, \mathbf{x}') = \langle \mathbf{u}(\mathbf{x}, t_k) \otimes \mathbf{u}(\mathbf{x}', t_k) \rangle_t \; , \tag{2.35}$$

where t_k and $\mathbf{x}$ are snapshot time and position vector, respectively. In POD, ϕ is chosen to maximize the value of $\left\langle |(\mathbf{u}, \phi)|^2 \right\rangle / \| \phi \|^2$, where $\langle \cdot \rangle_t$, $\langle \cdot \rangle$, $(\cdot, \cdot)$ and $\| \cdot \|$ are time average, spatial average, inner product and norm, respec-

tively. Since the spatial modes ϕ^l are orthonormal to each other, the following equation can be used

$$\phi^l(\mathbf{x}) = \sum_{k=1}^{N_s} a_k^l \ \mathbf{u}(\mathbf{x}, t_k) \ . \tag{2.36}$$

In order to determine the coefficients a_k, Eq. (2.36) is substituted into Eq. (2.34), resulting in

$$\left(\frac{1}{N_s} \sum_{i=1}^{N_s} \mathbf{u}(\mathbf{x}, t_i) \otimes \mathbf{u}(\mathbf{x}, t_i), \sum_{k=1}^{N_s} a_k \mathbf{u}(\mathbf{x}, t_k) \right) = \lambda \sum_{k=1}^{N_s} a_k \mathbf{u}(\mathbf{x}, t_k) \ ,$$

where N_s is the total number of snapshots. Sirovich [73] simplified this equation into

$$\sum_{k=1}^{N_s} \frac{1}{N_s} \left(\mathbf{u}(\mathbf{x}, t_i), \mathbf{u}(\mathbf{x}, t_k) \right) a_k = \lambda a_i \quad ; \quad i = 1, ..., N_s \ . \tag{2.37}$$

Equation (2.37) can be rewritten in symbolic form as:

$$\mathbf{C}\mathbf{A} = \lambda \mathbf{A} \, , \tag{2.38}$$

$$\mathbf{A} = (a_1, a_2, ..., a_{N_s})^T \, , \tag{2.39}$$

$$C_{ij} = \frac{(\mathbf{u}(\mathbf{x}, t_i), \mathbf{u}(\mathbf{x}, t_j))}{N_s} \ . \tag{2.40}$$

Solving this eigenvalue problem, Eq. (2.38), leads to a total of N_s eigenvalues, written λ^l, and eigenvectors, denoted $\mathbf{A}^l$ ($l \in 1, 2, 3, ..., N_s$). When using SPOD for data analysis or data compression, it is not always necessary to keep all N_s modes. Then, M represents the number of modes retained in the analysis while N_s still represents the total number of snapshots, i.e., the whole data-set available for the analysis, obviously with $M \leq N_s$.

2.6.2 Spectral Entropy

Equation (2.37) describes in general the eigenvalue problem based on the temporal autocorrelation function as kernel. The obtained eigenvalues represent the spectrum of the autocorrelation matrix ($\mathbf{C}$ in Eq. (2.38)). In order to

characterize the intensity of the turbulence contained in the analyzed velocity field $\mathbf{u}$, the spectral entropy S_d can be introduced. This quantity allows one to distinguish between different flow regimes, from "highly disordered" (here, meaning turbulence), to "partially ordered" (here, for transition), or "well ordered" (here, for laminar flow). For the computation of the spectral entropy, the relative energy P^l of mode l is first computed based on the corresponding eigenvalue, after ordering them in decreasing order based on λ^l, as:

$$P^l = \frac{\lambda^l}{\sum_{j=1}^{M} \lambda^j} , \tag{2.41}$$

where $M \leq N_s$ is the number of modes retained in the analysis. Then, the spectral entropy can be determined as:

$$S_d = -\sum_{l=1}^{M} P^l \ln P^l . \tag{2.42}$$

According to Eq. (2.42), the maximum possible value of S_d is reached when all eigenvalues are equal to each other, i.e., $P^l = 1/M$, and consequently $S_d = \ln(M)$. Physically, this means that the energy is equally distributed over all the M modes. The minimum value of S_d corresponds to the case where the original signal contains only a single mode, the first one, meaning that the flow field is steady. Then, $S_d = 0$.

Chapter 3

Large eddy simulation of the FDA benchmark nozzle

This chapter investigates the flow in a benchmark nozzle model of an idealized medical device using computational fluid dynamics (CFD). It was proposed by the Food and Drug Administration (FDA) [31]. It will be shown that a proper modeling of the transitional flow features is particularly challenging, leading to large discrepancies and inaccurate predictions from the different research groups using Reynolds-averaged Navier-Stokes (RANS) modeling [79]. In spite of the relatively simple, axisymmetric computational geometry, the resulting turbulent flow is fairly complex and non-axisymmetric, in particular due to the sudden expansion. The resulting flow cannot be well predicted with simple modeling approaches. Due to the varying diameters and flow velocities encountered in the nozzle, different typical flow regions and regimes can be distinguished, from laminar to transitional and to weakly turbulent. The purpose of the present chapter is to re-examine the FDA-CFD benchmark nozzle model at a Reynolds number of 6 500 using large eddy simulation (LES) [42]. The LES results are compared with published experimental data obtained by Particle Image Velocimetry (PIV) and an excellent agreement can be observed considering the temporally-averaged flow velocities. Different flow regimes are characterized by computing the temporal energy spectra at different locations along the main axis [17]. In order to reduce the computational costs, the performance of a hybrid simulation is investigated [17].

3.1 Introduction

The Food and Drug Administration (FDA) is responsible in the USA for the authorization and control of new medical devices. Their mission is to protect "the public health by assuring the safety, efficacy and security of human and veterinary drugs, biological products, medical devices" [1]. In this process results based on computational fluid dynamics (CFD) are becoming more and more important to demonstrate the efficacy and safety of new technologies and products. Though CFD is widely used and accepted in various engineering fields, the relevance and accuracy of CFD is still questioned in part of the biomedical community [50, 77]. This is one reason why FDA decided to propose a benchmark case to check the validity and accuracy of CFD predictions for a typical biomedical application (Fig. 3.1). A total of 28 CFD groups from all around the world have participated to this benchmark, performed the required computational steps and delivered the results for a later analysis [79]. Complementary experimental investigations [31] – using blood-analog fluids to match the refractive index of the acrylic geometry – were also performed using Particle Image Velocimetry (PIV) in order to generate a reference database for the CFD validation. However, the experimental results were not known prior to the simulations (blind predictive test). The aim of the FDA-study was to evaluate the current state of the art in CFD modeling in an idealized medical device model, specifically: "(1) develop a suitable benchmark model for the interlaboratory study (as well as for future research and standards development); (2) evaluate and compare each participants CFD simulations against quantitative flow visualization experiments carried out in three independent laboratories; and (3) extract needed input for the development of standards and guidelines for industry and FDA reviewers who employ or consider CFD in premarket device applications and postmarket investigations of device problems" [79].

Comparing the CFD results with the experimental data, large discrepancies were observed among the numerical predictions [79]. The discussed results involved both laminar as well as turbulent simulations for five different Reynolds numbers ranging from $\mathrm{Re} = 500$ to $\mathrm{Re} = 6\,500$, using as typical length-scale the throat diameter. The computational geometry is otherwise identical for all cases (Fig. 3.1).

The investigated configuration is axisymmetric and can in principle be computed as an axisymmetric domain without swirl (2D), greatly reducing the computational efforts. None of the contributed CFD results relied on large eddy simulation, probably due to the much higher computational effort. In-

[1] http://www.fda.gov/AboutFDA/WhatWeDo/

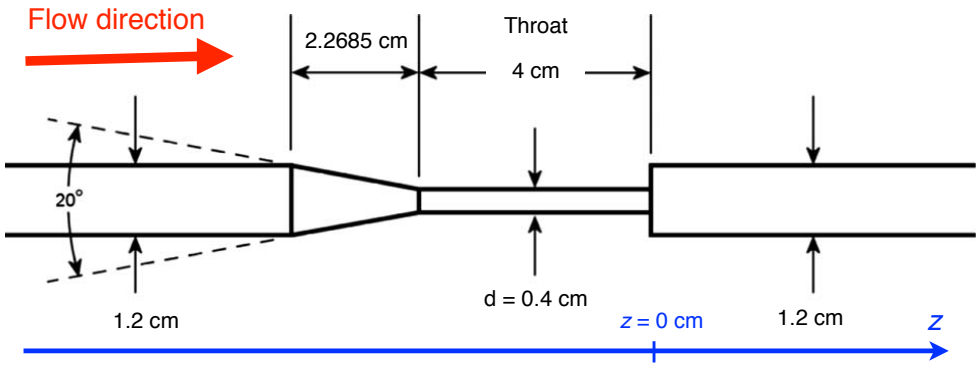

Fig. 3.1: Schematic representation of the computational domain for the FDA-benchmark nozzle model. [17] [31] [42]

stead, the CFD simulations discussed in [79] rely on laminar and Reynolds-averaged Navier-Stokes (RANS) models involving both steady and transient as well as two- and three-dimensional computations.

In their conclusion, the FDA-experts "do not endorse or recommend the use of any particular turbulence model over any other", raising in particular the question: could large eddy simulation outperform the presented laminar and RANS computations? In what follows only the highest Reynolds number considered in the FDA study (Re = 6 500) based on throat diameter is investigated using large eddy simulation [42]. This case is challenging since it clearly involves transition and noticing that "minor flow rate variations can have a substantial effect on the nature of the flow" [79]. This particular Reynolds number in the original study has been investigated by several groups, two of them assuming a laminar flow, the remaining ones using three different turbulence models, namely: Spalart-Allmaras in one case, $k-\omega$ in three studies, $k-\omega$ SST in 12 studies and $k-\epsilon$ in 10 computations.

For engineering applications at very high Reynolds numbers, it is very challenging to obtain the needed resolution in space and time. In the present case, the Reynolds number Re = 6 500 based on throat diameter is still moderate, so that a proper resolution can be obtained. The aim of the present chapter is thus to re-investigate the FDA benchmark nozzle using LES and check the accuracy of the obtained results [42].

3.2 Methods

3.2.1 Computational Mesh

In order to eliminate any spurious influence of the inlet and outlet boundary conditions, the considered geometry (Fig. 3.1) has been extruded at both ends of the considered domain, especially at the outlet. A previous test with a shorter domain has shown a recirculation at the outlet for the investigated Reynolds number. Therefore, the final computational domain is selected to be 9 cm long between the sudden expansion and the outlet, while the complete computational domain is almost 20 cm long.

The applied computational mesh needed for the finite-volume simulation has been generated using the commercial tool ICEM-CFD (Ansys Inc., Canonsburg, PA, USA). The block-structured mesh involves 9 129 600 finite-volume cells composed of hexahedral elements using two combined O-grid topologies [42]. An example of the computational mesh used for the present case is shown in Fig. 3.2. For all the mesh elements the orthogonal quality is better than 0.7 (1 being the highest) and the equi-angle skewness is better than 0.5 (1 being the worst and 0 the optimum), leading to an excellent overall mesh quality.

The volume of the smallest grid volume elements, which are found in the region near the expansion, is 1.5×10^{-5} mm^3, corresponding to a cell size of $24 \times 24 \times 25$ μm. An extremely fine resolution has been implemented in the vicinity of the walls. The wall normal grid distance is between 7.5 and 27.5 μm providing a near-wall resolution less than one in wall units [42].

The largest computational cells are located near the inlet and outlet. The resolution is gradually refined approaching the two ends of the throat section. An extremely fine resolution is provided at the level of the sudden expansion, which has been found to be very important in order to resolve correctly the flow separation [42]. The boundary layer is fully resolved in the present work and is thus not modeled as common in a RANS approach. This direct resolution is hardly possible for high Reynolds numbers, but is feasible for a moderate Reynolds number as in the present case. The final mesh resolution is mainly guided by the wall resolution and having almost homogeneous cells in the core of the domain.

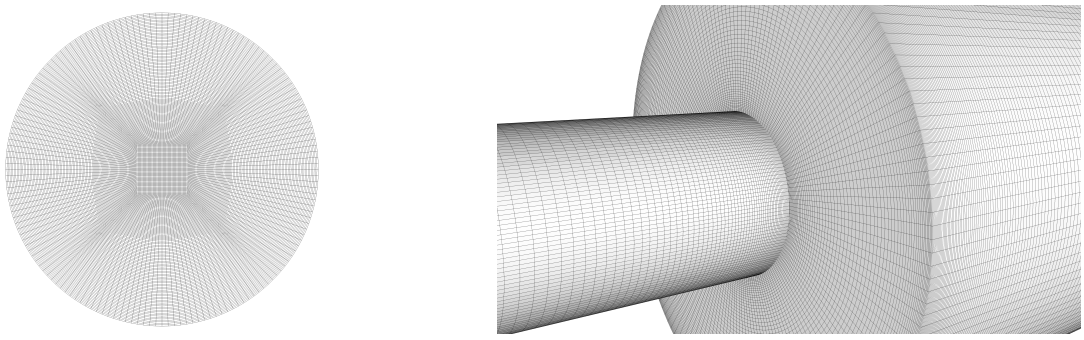

(a) (b)

Fig. 3.2: Block-structured computational mesh for the FDA benchmark nozzle (a) two combined O-grid topologies at the outlet of the domain (b) refined mesh near the sudden expansion. [42]

3.2.2 Computational Details

The fluid flow simulations have been performed using the commercial finite-volume solver ANSYS Fluent 14 (Ansys Inc., Canonsburg, PA, USA) applying the double-precision pressure-based solver [42].

The inlet boundary condition for the velocity is prescribed in the form of a steady laminar parabolic profile. Note that the Reynolds number computed from the entry diameter is only $\mathrm{Re} = 2\,167$, denoting laminar conditions and therefore justifying this assumption. As a consequence, the observed complex unsteady flow downstream the sudden expansion is directly a result of the local flow instability associated to transition ($\mathrm{Re} = 6\,500$ when computed with the throat diameter).

Traction-free conditions are implemented at the outlet, assuming an identical uniform relative pressure. A standard, no-slip boundary condition is employed along the walls. [42]

The fluid is represented using isothermal and incompressible Newtonian blood properties. The constant density and the dynamic viscosity are chosen as 1056 $\mathrm{kg/m^3}$ and as 3.5 $\mathrm{mPa \cdot s}$, respectively [79].

Computations are carried out in parallel using 32 Linux computing cores on eight quad-core computing nodes equipped with AMD Opteron 64-bit Processor 2352 having 2.1 GHz clock rate. Each node has 32 GB memory and the internode communication is realized with a high-speed InfiniBand connection. For the mesh considered in this study, over 20 GB of computer memory are needed for the simulation. The complete numerical simulations are finished

in around 470 hours wall-clock-time, corresponding to almost 20 days on 32 computing cores in parallel. [42]

The time advancement is realized using the Non-Iterative Time Advancement (NITA) based on the Fractional Time Step method with an implicit second-order scheme.

The convective terms in the momentum equations are discretized with a second-order central differencing scheme and the Least Squares cell-based approach is employed for the interpolation of variables on cell faces.

A constant time step of 10^{-5} s ensures that the Courant-Friedrichs-Lewy (CFL) number is less than unity everywhere. Before starting the averaging procedure in time, the simulation was continued for more than 50 000 time steps, corresponding to three through-flow times from inflow to outflow of the computational domain. All the presented profiles are the results of time-averaging performed during 100 000 time steps (almost 7 through-flow times), ensuring converged statistics. [42]

3.3 Results

Exemplary instantaneous velocity magnitudes are shown in Fig. 3.3(a). A computed iso-surface of the Q-criterion for $Q = 2 \times 10^6$ 1/s colored with the same axial velocity is shown in Fig. 3.3(b). The topology of this quantity reveals the existence of strong coherent structures in the considered flow showing a periodic street of vortex rings downstream the nozzle. Fig. 3.4(a) shows the instantaneous velocity magnitudes in a two-dimensional cut in the middle of the geometry. The high velocity regions shown in red color downstream the sudden expansion reveal the coherent ring-shaped structures produced periodically. Fig. 3.4(b) presents the computed vorticity magnitude in the same cut plane and at the same time step, showing the jet flow and highlighting the strong interaction between the near-axis high-speed jet and the stagnating flow in the recirculation.

These figures illustrate the complexity of the turbulent structures induced by the sudden expansion in this rather simple geometry. The resulting, highly unsteady flow cannot be directly compared with transient experimental results, because of the stochastic nature of turbulence. Nevertheless, all the realizations should give the same results in a statistical sense. Therefore, the temporally-averaged computational results are compared next with the averaged experimental results.

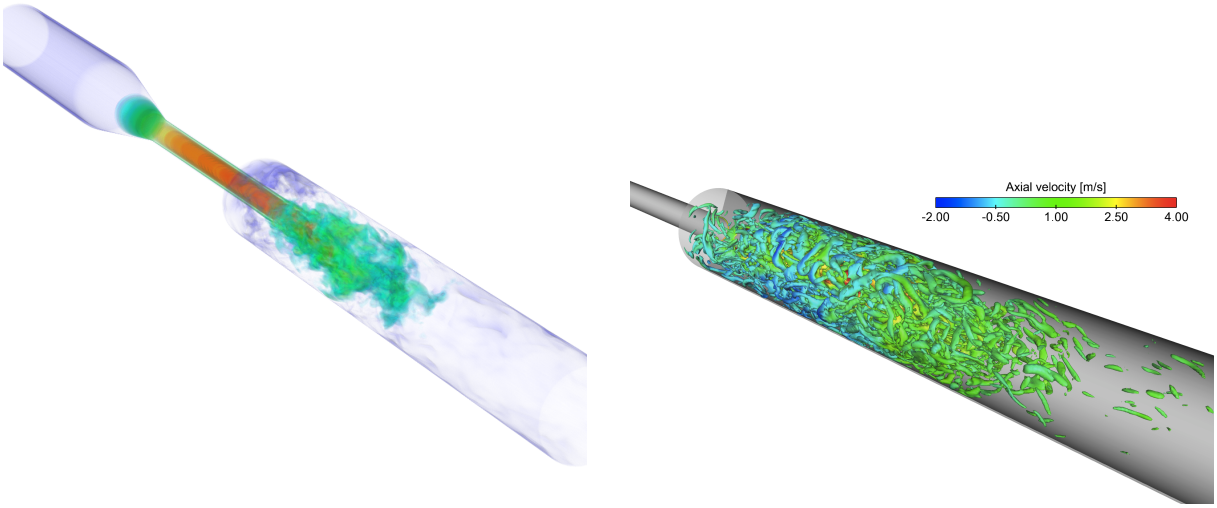

(a) (b)

Fig. 3.3: Various representation of the instantaneous turbulent flow at Re = 6 500 in the nozzle. (a) Volume rendering of instantaneous velocity magnitude and (b) corresponding iso-surface of the Q-criterion colored by the axial velocity. [42]

Experimental data have been obtained by independent PIV measurements in three different laboratories [31]. As discussed in [31], the different groups observed either laminar or transitional flows even before reaching the throat for the considered Reynolds number. These different observations for the same configuration point out to one of the main difficulties of the present case. While Re = 6 500 corresponds clearly to turbulent conditions in the throat section, the corresponding Reynolds number computed with the diameter of the baseline pipe is Re = 2 167, very close to the value associated to transition ($\mathrm{Re}_c \approx 2\,300$), so that laminar or transient conditions might be found due to spurious effects, like slight vibrations in the surroundings. Even very small disturbances might be amplified and lead to different experimental observations.

All experimental results shown in what follows, for instance in Fig. 3.5, are the averaged values obtained by the three laboratories reported in [31]. The error bars represent the deviation between the different measurements (min-max range). Fig. 3.6 depicts the computed time-averaged axial velocity along the centerline [42]. The symbols illustrate the average of all PIV experiments. The deviation is again shown by error bars.

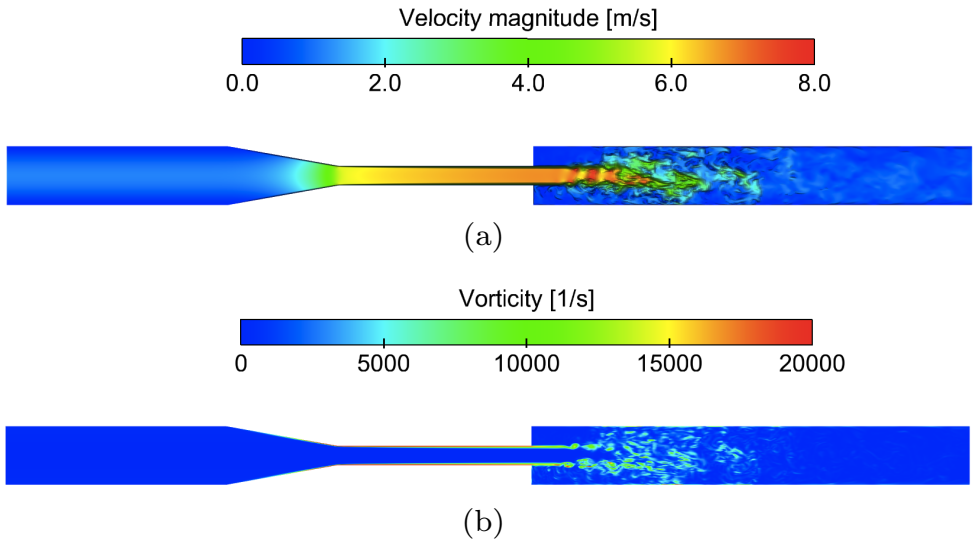

Fig. 3.4: Instantaneous turbulent flow at Re = 6 500 in the middle plane of the nozzle. (a) instantaneous velocity magnitude in a two-dimensional cut-plane and (b) corresponding values of vorticity magnitude. [42]

In the present computations a steady laminar inflow (parabolic) profile is prescribed at the inlet of the domain. No artificial turbulence fluctuations are superimposed at the inlet, as it is often required for LES computations at high Reynolds numbers. Hence, all the unsteady flow features observed downstream are solely a result of transition within the considered geometry. [42]

Most of the temporally-averaged axial velocity profiles show fully symmetric curves (Fig. 3.5). For the last two measured sections ($z = 0.060$ and $z = 0.080$ m in Fig. 3.5) velocities are not yet fully symmetric, despite of the long averaging time [42]. Indeed, these profiles are located in the relaminarization region. Because the Reynolds number there is very close to the critical Reynolds number, the full relaminarization of the flow takes a considerable time and could only be observed further downstream, leading to exceedingly high computational costs.

3.3.1 Turbulent Velocity Spectra

In order to characterize the different flow regimes, turbulent spectra are now investigated. Various probe locations along the centerline of the geometry have

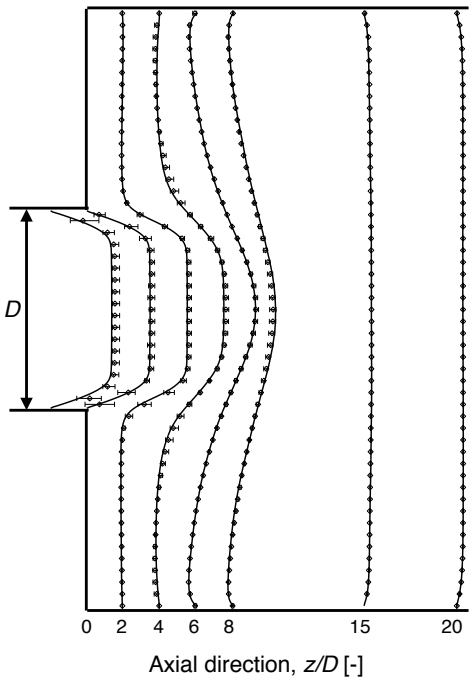

Fig. 3.5: Time-averaged axial velocity compared with PIV measurements along various cuts near the sudden expansion. Experimental values are plotted with symbols, solid lines represent the averaged, resolved axial velocities obtained by LES. For a better visibility, only a part of the computational domain is considered. [42]

been defined. At these points the instantaneous axial velocity components are stored during the last 10 000 computational time steps. The first probes (left part of Fig. 3.7) are placed before the convergent nozzle, and no oscillations are visible. The next probes, located within the convergent nozzle, show a slight periodic oscillation with amplitude modulation. Then, the probes located downstream the sudden expansion (at $z = 0$) show clearly unsteady transitional behavior, before relaminarization occurs (right part of Fig. 3.7). [42]

The corresponding spectra of turbulent kinetic energy have been computed at these same locations and are shown in Fig. 3.7. These logarithmic plots illustrate the turbulent kinetic energy as a function of the Strouhal number St. Spatial correlations are usually presented as a function of the wave number, while the temporal correlations are plotted against the frequency or Strouhal number. According to Kolmogorov [51] the energy spectra can be well ap-

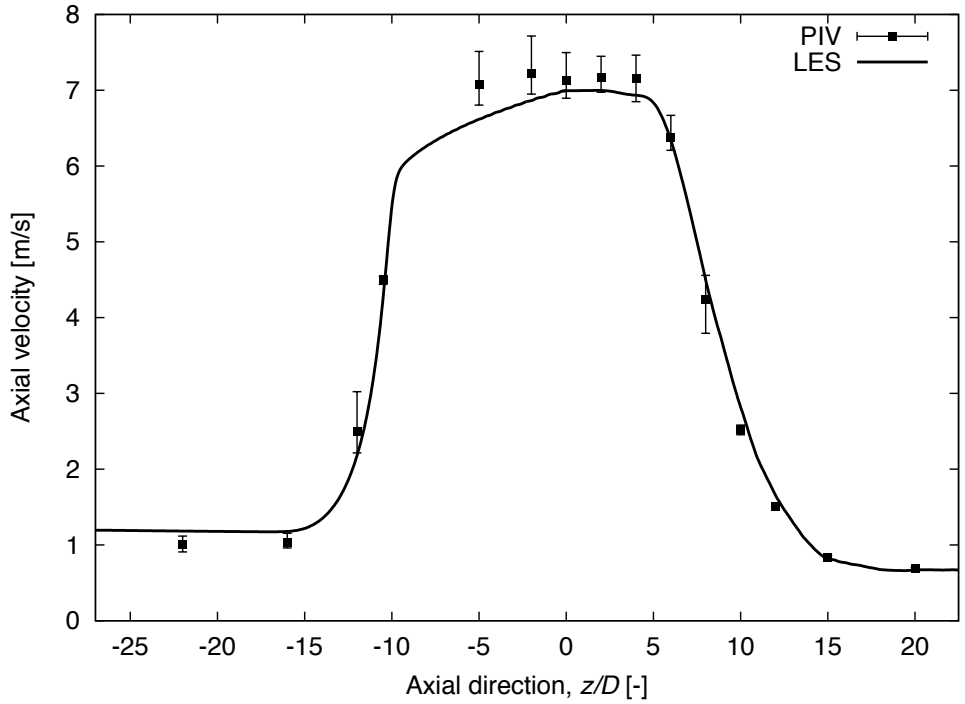

Fig. 3.6: Time-averaged axial velocity compared with PIV measurements along the centerline. Experimental values are plotted with symbols, the solid line represents the averaged, resolved axial velocity obtained by LES. [42]

proximated with a $-5/3$ slope [38] in the so-called inertial subrange for high Reynolds numbers. [42]

The constant laminar values at the first probes do not lead to any noticeable turbulent kinetic energy content, as expected. Within the throat, the induced slight oscillations are associated with a limited amount of kinetic energy in Fig. 3.7, indicating the onset of the transitional stage of the flow. Downstream of the sudden expansion, the flow is clearly turbulent, and part of the spectra can be very well approximated with a slope of $-5/3$, even if a large part of it can be still better described by a slope of $-10/3$. Far from the sudden expansion the kinetic energy decays and the obtained spectra show a decreasing amount of energy. The $-10/3$ slope becomes more and more important in these region, representing the viscous dissipation subrange indicating high-frequency turbulent motions. [42]

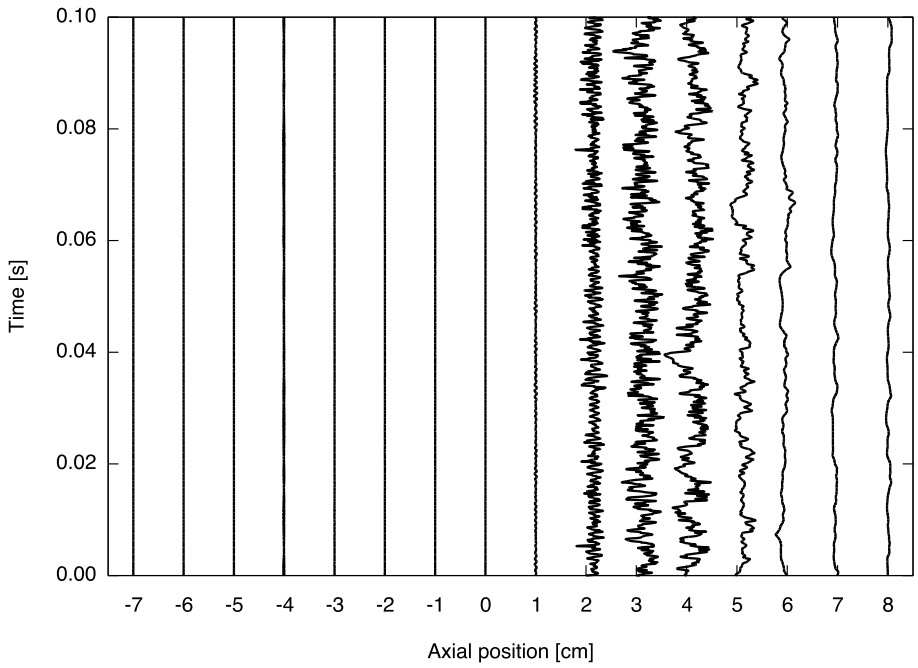

Fig. 3.7: Instantaneous axial velocity values at various locations along the centerline. [42]

3.4 Discussion

The presented results are not obtained from a blind test as those discussed in [79]. The measurement results were available before starting the LES computations. However, no modification of the models was needed to improve the comparisons. The results are obtained using a high-quality, well-resolved mesh with appropriate time steps, and this was found to be sufficient. No further parameters – e.g., the Smagorinsky constant – had to be adapted in order to improve the results.

The temporally averaged axial velocity profiles have been obtained experimentally by PIV [31]. These results could not be well reproduced by any of the RANS simulations discussed in [79]. Here, as observed when looking back at Fig. 3.5, a truly excellent agreement can be observed in all regions of the geometry, before, within and after the throat. In particular, the obtained LES results predict well the velocity profiles after the sudden expansion, in spite of the complex turbulent nature of the fluid flow illustrated for instance in Fig. 3.3.

It is known that symmetric diffusers may lead to separation on one side and attachment on the other side. Therefore, a non-symmetric flow can develop within a truly axisymmetric configuration. This might be a problem for the considered benchmark nozzle and explain why the transient and turbulent flows are not always axisymmetric, as shown exemplary in Fig. 3.3. This might also be one reason for the poor agreement with experimental data documented in [79], since this behavior obviously cannot be predicted by two-dimensional axisymmetric computations.

Another reason for the discrepancies discussed in [79] is that unsteady RANS simulations cannot really predict all the different flow regimes encountered in the considered application, from laminar to turbulent through transition. A wall-resolved LES based on the standard Smagorinsky model [74] model with wall damping delivers an excellent agreement compared with experiments in the present study.

The velocity spectra obtained in the current simulation have been presented in Fig. 3.7. The observation are consistent with the $-5/3$ power law representing the inertial range in the theory of Kolmogorov, even if this applies only to a small region. The largest part of the spectra beyond the sudden expansion can be well represented with a slope around -3 or $-10/3$ [42]. A slope of $-10/3$ has been observed experimentally for stenotic conditions at relatively low Reynolds numbers [57]. Molla et al. [60] reported a combination of slopes $-5/3$ and $-10/3$ in a modeled stenosis using LES computations. They observed that the slope of $-10/3$ was more pronounced in the relaminarization regime. In the current work the kinetic energy spectra are mostly characterized with the slopes of $-5/3$ and $-10/3$, showing that even small-scale vortical structures appear to be well resolved.

These observations demonstrate that the resolution of the employed LES computations is sufficient.

3.5 Hybrid Simulations

Hybrid simulations might be very interesting to save computational resources for a variety of applications involving different flow regimes. Combining proper models for laminar, transitional, or turbulent flows, described either by steady RANS, unsteady RANS (URANS), LES or DNS depending on the needs, an accurate solution could then be obtained for complex configurations on existing computers. To do so, it is necessary to decide which kind of model should be used in which part of the numerical domain in space and time. As shown

in this chapter, the spectral entropy S_d obtained from solving the eigenvalue problem for the temporal autocorrelation function, can be used in order to uniquely and automatically quantify the flow state and differentiate between laminar, transitional, or turbulent regime; as such, it delivers a direct measure of turbulence intensity. Using S_d, an URANS/LES hybrid simulation have been carried out for the blood nozzle benchmark proposed by the FDA. Savings in computational time and disk storage is observed, while keeping a very high accuracy [17].

A criterion allowing to uniquely and automatically quantify the flow state and differentiate between laminar, transitional, or turbulent regime is essential to guide hybrid simulations, combining in the best possible way different simulation models (laminar flow equations; Reynolds-averaged Navier-Stokes approach – RANS; Unsteady RANS – URANS; Large Eddy Simulations – LES; Direct Numerical Simulations – DNS;...). After identifying the flow state and quantifying turbulence intensity, a suitable approach can be implemented in an adaptive manner to combine proper models in space (different regions being computed using different numerical models), as shown in [18]); and/or possibly in time, switching between different computational approaches as appropriate. Considering the rapid development of hybrid simulations [72], identifying automatically the most appropriate model is becoming increasingly important. In order to be successful, hybrid simulations should ultimately rely on a user-independent and generally valid indicator of the flow state computed from the simulated flow field, as proposed in this work. Additionally, such an indicator could readily be used to guide in an automatic manner the resolution needed in space and time, so that, starting from a well-resolved – but time-consuming – computation, grid coarsening and/or larger time steps could be used for part of the domain or the simulation, similar to what is done for embedded DNS [16]. Finally, the same approach could also be used to automatically detect regions of interest (e.g., places where transition takes place) when analyzing large datasets. Such a procedure would be valuable for a variety of biomedical flows, in which laminar, transitional and turbulent regions are often found simultaneously, with considerable impact on clinical outcome [14].

3.6 URANS/LES Simulation of the FDA Blood Nozzle

In order to check the performance of URANS/LES hybrid simulations the benchmark nozzle [79] is considered. Five different Reynolds numbers ranging from $\mathrm{Re} = 500$ to $\mathrm{Re} = 6\,500$ were proposed, computed using the throat

diameter as typical length-scale. Laminar and RANS models were not able to deliver acceptable results. Subsequent studies have been able to achieve a much better agreement using LES [20, 42, 87], but obviously at a much higher computational cost. For the present study, the case with Re = 6 500 is selected, since it is the most challenging one from the point of view of the flow state.

3.6.1 Computational Setup

In order to deliver meaningful comparisons, the same simulation is executed twice, once relying completely on LES, and a second time starting with LES and switching to the hybrid URANS/LES approach based on the S_d indicator. For both simulations, the original setup is based on the recommendations of [42]. All simulations have been performed using the finite-volume solver ANSYS Fluent 17 with the pressure-based solver [17]. The fluid is specified to be isothermal, incompressible and Newtonian. Concerning density and viscosity, 1056 kg/m^3 and 3.5 mPa·s are set, respectively, following the recommendations of the FDA challenge [31]. For the hybrid simulation, the Stress-Blended Eddy Simulation (SBES) approach is applied. In this approach, the user can provide the definition of the shielding function (f_{SBES}) [17]. This will decide which model is activated in a specific region by computing the turbulent viscosity:

$$\nu_t^{SBES} = f_{SBES}\nu_t^{URANS} + (1 - f_{SBES})\nu_t^{LES} \ . \tag{3.1}$$

A value of 1 specifies a URANS region (using here the $k-\omega-$SST model), while a value of 0 denotes a LES region. For our application, the shielding function is defined based on the value of the spectral entropy, with $f_{SBES} = 0$ when $S_d \geq S_{d,crit.}$, where $S_{d,crit.}$ is the critical spectral entropy. Previous studies relying on Direct Numerical Simulations have shown that a spectral entropy around 0.46 represents the onset of transition. In order to stay on the safe side, a lower threshold of $S_{d,crit.} = 0.25$ is retained here, ensuring that LES is activated early enough for properly representing transition; this is impossible with a URANS approach.

The pure LES simulation corresponds simply to $f_{SBES} = 0$. In this way, one can use exactly the same setup for the LES and hybrid simulations; only the mesh and the shielding function have to be replaced.

At the nozzle inlet, a steady laminar parabolic velocity profile is prescribed, as the Reynolds number computed for the entry diameter is 2 167, which is below the critical Reynolds number for pipes. However, a very low (0.5%) tur-

bulence intensity was added, as proposed by [87]. In their study, they found that this improved the prediction of transition. Concerning the turbulence length scale, $0.07d_{pipe}$ is specified following users' guidelines. The outlet is defined as a pressure outlet. All walls are defined with standard no-slip boundary condition.

The Non-Iterative Time Advancement solver is chosen with the Fractional Step method. Instead of the second-order implicit temporal discretization, as done by [42], the bounded second-order implicit scheme is retained, since this is required by SBES. To ensure an appropriately small CFL number, the time step is chosen to be constant at 10^{-5} s. [17]

3.6.2 LES and Hybrid Simulations

For the wall-resolved LES simulations, a fully structured hexahedral mesh is created with 18 million cells composed of hexahedral elements using two combined O-grid topologies. It is checked that the condition $y^+ \approx 1$ holds everywhere at the walls. The domain covers $z \in [-108; 180]$ mm, where $z = 0$ is the location of the sudden expansion in the blood nozzle. To initialize the flow-field, 30 000 time steps are first executed. Afterwards, the computation is pursued until reaching 100 000 time steps. The obtained average velocity profiles indicate a very good agreement with the experimental data and with the previous numerical study, see Fig. 3.10. [17]

In order to carry out the spectral entropy analysis, the hybrid simulation is started in exactly the same way, using the same mesh (18 million cells) with LES. Between time steps 10 000 and 13 000 time steps, every 10^{th} time step are exported for SPOD analysis. For the spectral computation, planar sections are defined perpendicular to the centerline at the discrete positions $z = [-100, -90, ..., 170, 180]$ mm. In each section, the instantaneous velocities are exported on a grid with resolution of 0.48 mm, resulting in the wider sections in 462, in the thinner sections in 52 data points. Finally, spectral entropy is computed as described in Subsection 2.6.2. The computation requires less than a minute. The result can be seen in Figure 3.9.

Based on S_d, the LES region is found to be in the region between 4 and 100 mm (Fig. 3.9); all other regions will switch to URANS mode. Of course, in URANS regions, a much coarser resolution is sufficient. Therefore, a second structured mesh is generated. It contains 9.5 million hexahedral cells, keeping the same resolution as previously within the LES region, but with a coarser mesh in the two URANS domains. After replacing the mesh, the simulation is

restarted until reaching again 100 000 time steps, activating the Vortex Method [8] along the URANS-LES interface to generate velocity variations as input to LES based on the URANS turbulence intensity. [17]

3.6.3 Comparisons

All experimental results shown in what follows are the averaged values obtained by the three laboratories, as reported in [31]. The error bars (in Fig. 3.10) or the grey corridor (in Fig. 3.11) represent the deviation between the different measurements (min-max range). Figure 3.10 shows the computed time-averaged axial velocity along the centerline obtained by LES and hybrid simulation. The agreement of the pure LES simulation with the measurements is very good. Even more important, the agreement of the hybrid simulation with PIV in the central pipe is only slightly worse than with pure LES; it is at least as good in all other flow regions; and this good agreement is obtained at a reduced computational cost. [17]

The available radial velocity profiles measured by PIV are compared with LES and hybrid simulation in Fig. 3.11. The agreement is very good in all cases. Due to the impact of URANS in the hybrid simulation, the obtained curves are slightly more symmetrical compared to the pure LES, and are therefore even closer to the PIV measurements. This is an indication that the averaging process is probably not completely finished yet in the pure LES simulation, while it is already attained in the hybrid simulation. This additional advantage is not reflected in the following runtime comparison. [17]

Both simulations have been carried out on the same system using 8 computer nodes, each equipped with a hexa-core Intel Xeon E5-1560v3 3.5 GHz processor, with a Gigabit Ethernet interconnection. Altogether, the run time was reduced by only 14%. Comparing only the last 70 000 time steps, a speed-up of 19% is observed. Repeating the last 1 000 time steps on a single node with both approaches, the runtime was found to be proportional to the mesh size, leading now to a speed-up by 45% (almost a factor 2). Hence, the somewhat disappointing speed-up is due to the parallelization approach retained in ANSYS Fluent, possibly in combination with the slow (Gigabit Ethernet) processor interconnection. In order to solve such issues, access to the code sources is necessary. [17]

3.7 Summary

The main motivation of this chapter was to investigate the turbulent fluid flow in the benchmark nozzle with a sudden expansion initially proposed by the FDA. The obtained results are compared in a quantitative manner with PIV measurements. An excellent agreement is observed [42]. Even if the current test was not blind as in the original study in [79], no model parameter had to be adapted in order to improve the obtained agreement.

Spectral entropy S_d has been used to delineate between laminar, transitional and turbulent conditions for a nozzle benchmark. Based on S_d obtained at high resolution, coarser meshes and simpler models have been activated in a hybrid simulation, combining URANS/LES for the investigated nozzle configuration. A close agreement is observed in the region of interest between the reference solution and the hybrid simulation results. A noticeable saving in storage is also observed, directly connected to the coarser mesh employed for the hybrid approach. On the other hand, the observed savings in terms of computing time are still limited: up to 19% for the presented blood nozzle. [17]

Parallelization and algorithmic issues on a non-regular grid have been identified as the main reason for this somewhat disappointing result. To get the best out of hybrid simulations, efficient parallel algorithms, fast communication networks and efficient load-balancing techniques must be implemented.

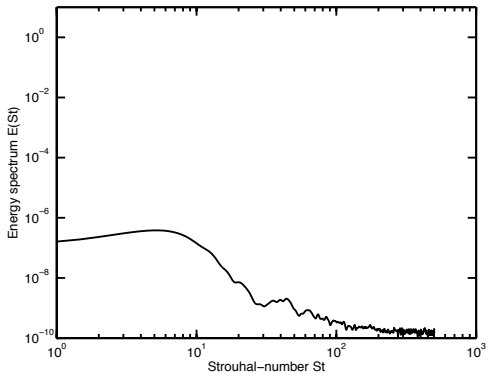

(a) $z = -7$ cm

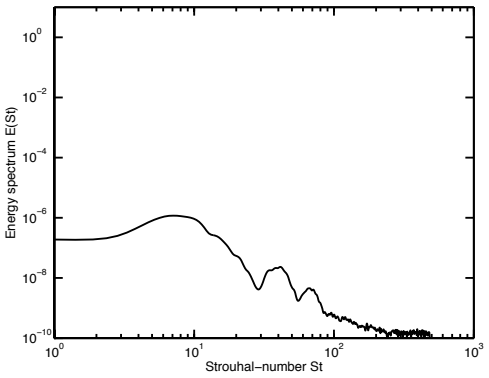

(b) $z = -6$ cm

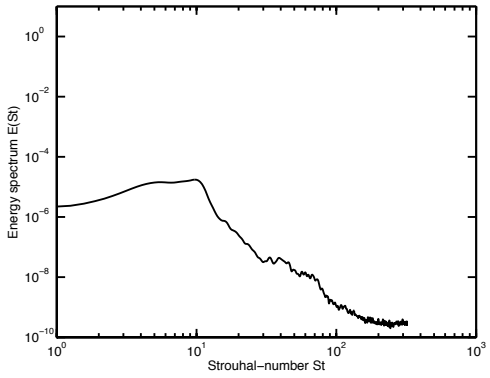

(c) $z = -5$ cm

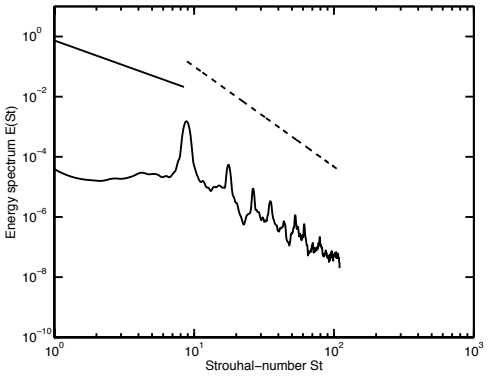

(d) $z = -4$ cm

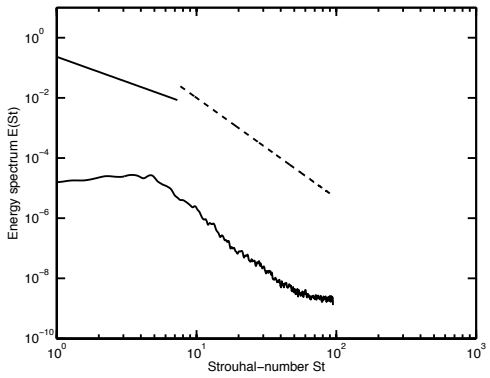

(e) $z = -3$ cm

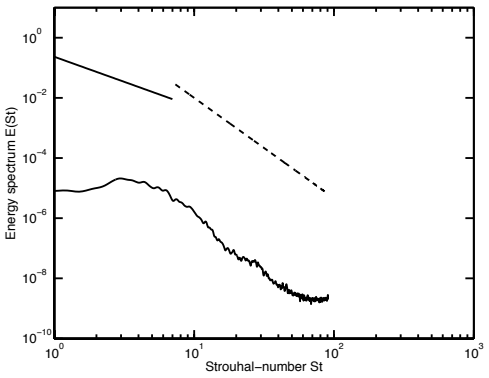

(f) $z = -2$ cm

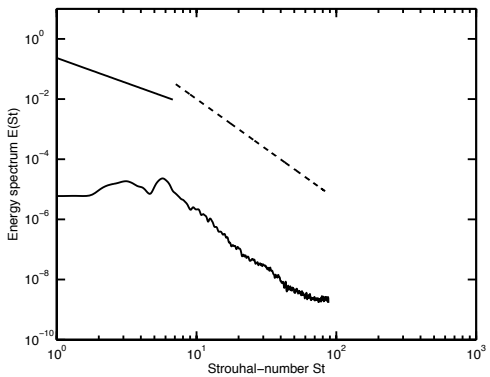

(g) $z = -1$ cm

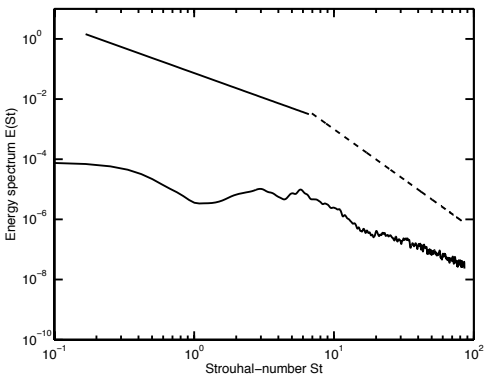

(h) $z = 0$ cm

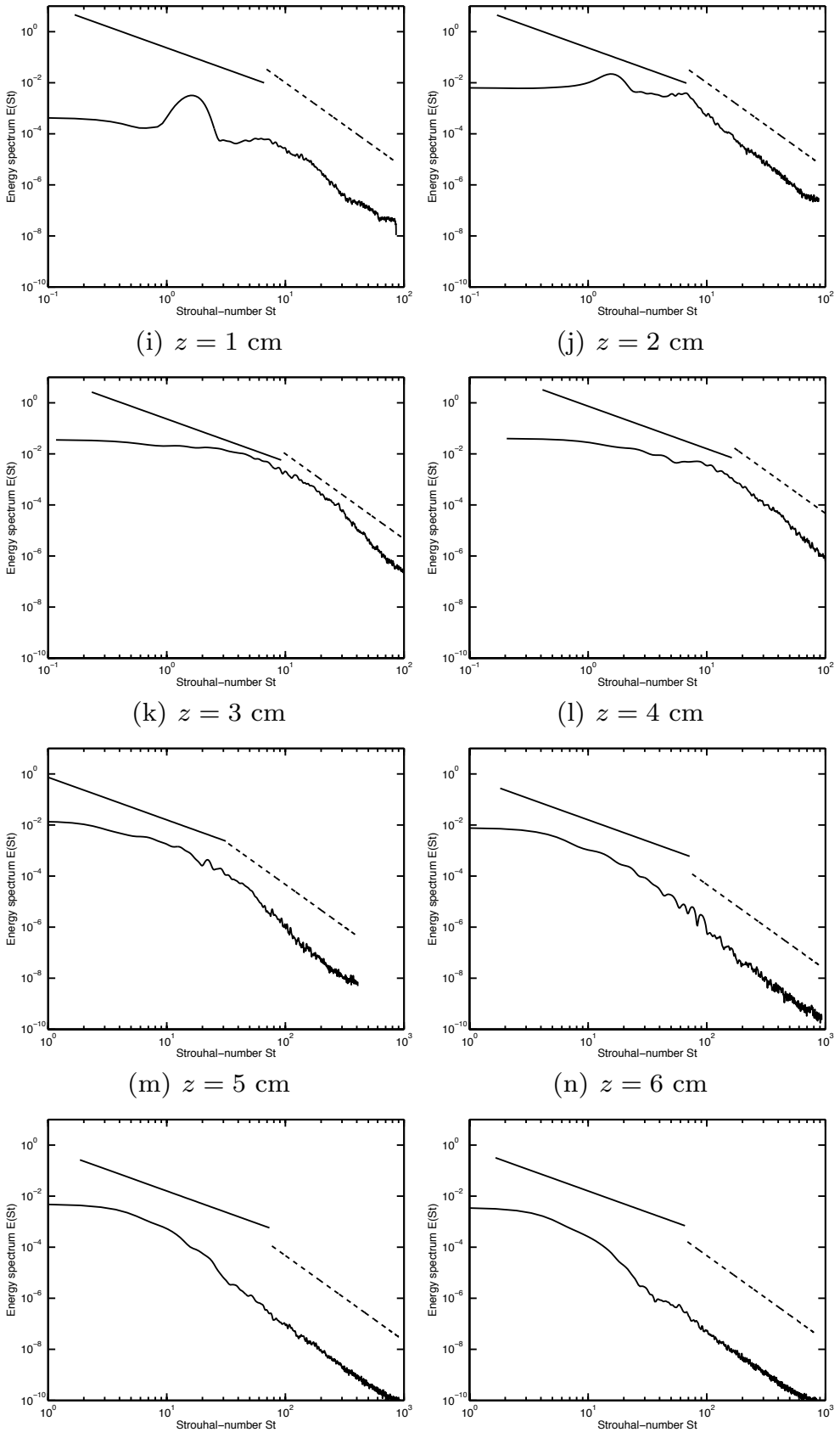

(i) $z = 1$ cm (j) $z = 2$ cm

(k) $z = 3$ cm (l) $z = 4$ cm

(m) $z = 5$ cm (n) $z = 6$ cm

(o) $z = 7$ cm (p) $z = 8$ cm

Fig. 3.7: Turbulence spectra of the resolved turbulent kinetic energy at various z-positions along the centerline. Straight solid lines show the $-5/3$ slope (corresponding to fully developed turbulence) and thick dashed lines correspond to the $-10/3$ slope (corresponding to the viscous dissipation subrange). The locations shown corresponds to the probes depicted in Fig. 3.7. [42]

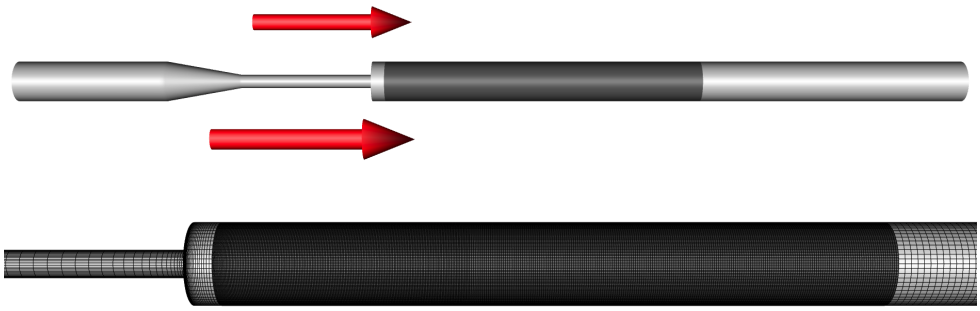

Fig. 3.8: Hybrid configuration for the FDA benchmark nozzle. In the top figure the LES region is highlighted as dark gray. The bottom figure shows the corresponding mesh on the nozzle wall surface. [17]

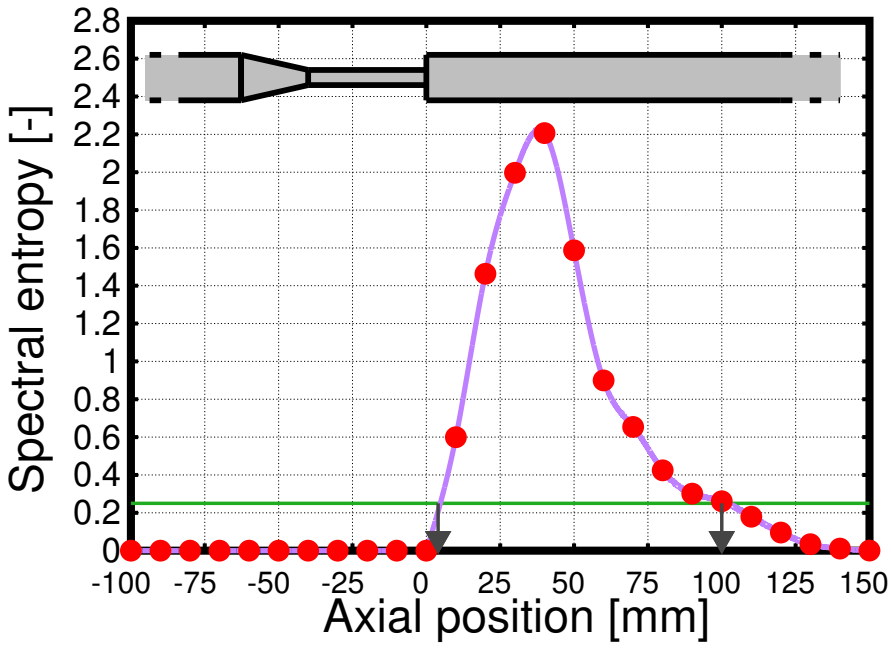

Fig. 3.9: Spectral entropy along the axial position (based on the LES results within the time interval $[0.1, 0.13]$ s). [17]

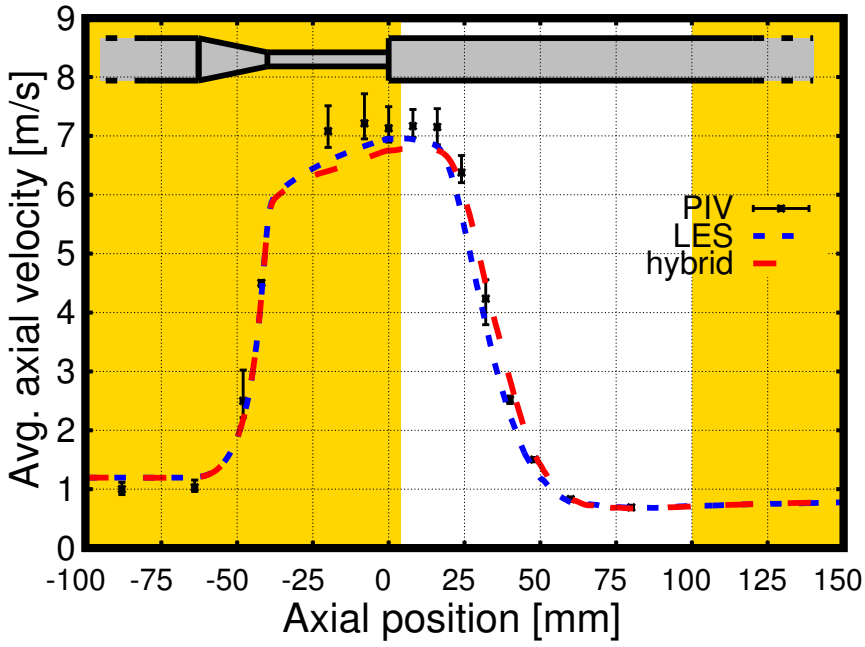

Fig. 3.10: Averaged axial velocities along the centerline (the yellow region denotes URANS domains in the hybrid simulation). [17]

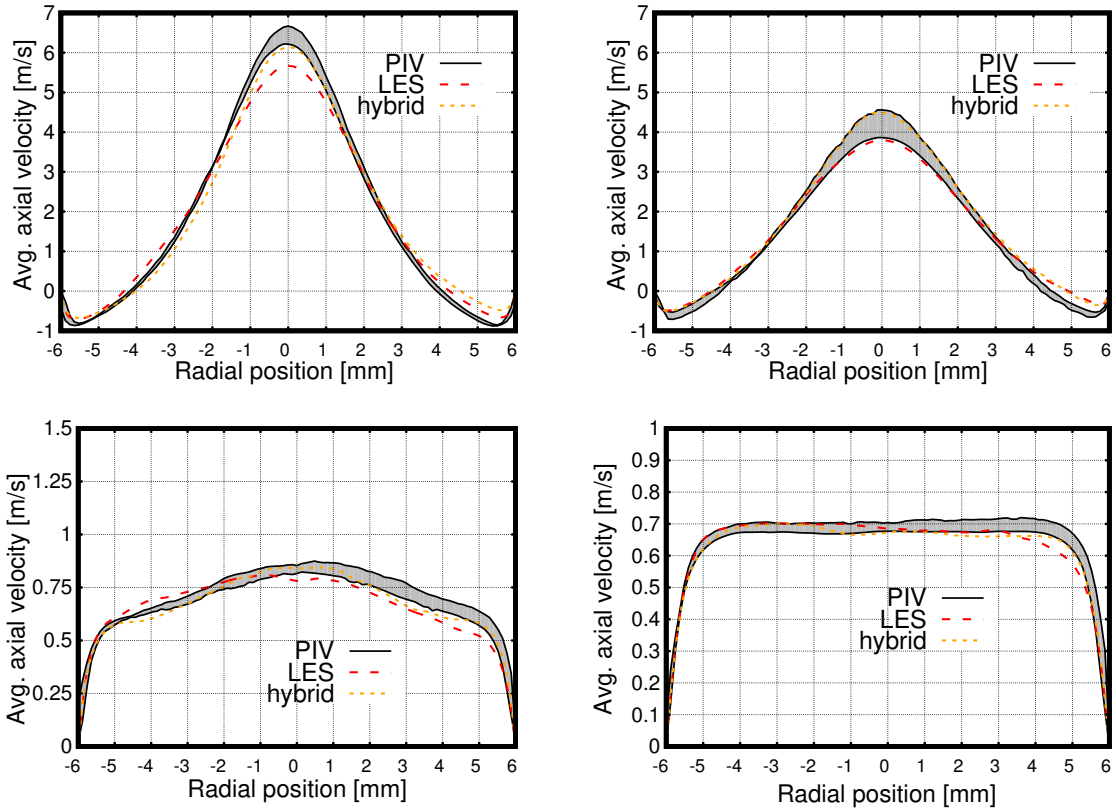

Fig. 3.11: Averaged axial velocities along the cross-section at $x/D = 6$ (top left), $x/D = 8$ (top right), $x/D = 15$ (bottom left), $x/D = 20$ (bottom right), compared to PIV experimental data (grey corridor). [17]

Chapter 4

Large Eddy Simulation of a Rotating Mixer

The present chapter examines the time-dependent three-dimensional hydrodynamics in a stirred tank reactor using computational fluid dynamics (CFD). The rotating propellers produce a complex, unsteady, three-dimensional turbulent flow field. This results in efficient mixing and is therefore widely used in various process engineering applications. The time-dependent turbulent single-phase flow is computed using large eddy simulation, relying on the sliding mesh approach [43]. The unresolved subgrid scales are treated using the Smagorinsky-Lilly model. The dominant coherent flow structures are characterized in the entire three-dimensional computational domain using the 3D proper orthogonal decomposition (POD) technique. The design of the propeller is evaluated in a separate POD analysis in a rotating frame, which encloses the propeller. The most energetic POD modes characterize the organized large scale structures, the so-called coherent flow structures, while the higher modes correspond to the small-scale disorganized turbulence. It was found that the dynamics of the main flow structures can be reconstructed using only 3 modes corresponding to 98% of the overall energy in the entire 3D inner rotating domain and 21 modes are necessary for the same amount of energy in the outer stationary region. [43]

Furthermore, the macro-instability (MI) is characterized by monitoring the velocity in more than one million computational cells, as well as using FFT analyses of the three-dimensional POD temporal coefficients. In the outer

stationary domain, both approaches showed characteristic frequencies around one-eighth and one-fifth of the blade passage frequency. [43]

4.1 Introduction

Stirred tanks are widely used in chemical and process engineering applications, as a large amount of chemical products are produced in such devices. The mixing process is predominantly controlled by the fluid flow. Therefore, the detailed understanding of the hydrodynamics is essential in order to further improve the mixing and hence influence product quality.

The hydrodynamic quantities can be investigated either experimentally or by means of numerical simulations. Laser-Doppler Velocimetry (LDV), Particle Image Velocimetry (PIV), or Particle Tracking Velocimetry (PTV) are well-established experimental methods used to determine the fluid flow velocities, however, their application is limited to optically-accessible regions. Furthermore, reflection might hinder the application of these optical systems, which is particularly true for geometries with curved surfaces such as cylindrical tanks.

Magnetic Resonance Imaging (MRI) is a relatively new method used to characterize flows in engineering applications. Phase-contrast MRI (PC-MRI) does not require the employment of transparent geometries and measurements in opaque fluids is also possible. However, the application of magnetic elements are not permitted in the measurement region. The signal-to-noise ratio can be improved for repetitive signals, therefore, it is well-suited for periodic flows [46].

On the other hand, numerical simulations can, in principle, resolve the detailed three-dimensional time-dependent flow as well as the turbulent quantities. Nevertheless, predictive physical models are absolutely necessary, especially if small-scale turbulent flow structures are incorporated in the analysis.

A careful inspection of the published studies reveals that fairly few attempts have been made to analyze the three-dimensional turbulent flow structures in stirred tanks. Therefore, the present study investigates the time-dependent three-dimensional turbulent fluid flow in a stirred tank agitated by a three-blade propeller without baffles on the tank wall. [43]

4.1.1 Proper Orthogonal Decomposition (POD)

Proper orthogonal decomposition (POD) is a relatively new technique employed to post-process a large amount of experimental or numerical data in fluid dynamics. Using this approach, the most dominant dynamic effects of the investigated variable – typically flow velocity – are extracted and projected on a subset of the state space. The obtained modes of the system are time-invariant and they represent the most persistent structures in the system. POD allows for the analysis of the complex temporal-spatial dynamics of the flow and the determination of the most energetic flow structures, the so-called coherent flow structures, responsible for a significant amount of kinetic energy. These characterize the large-scale organized flow structures. The higher POD modes represent the small-scale disorganized turbulence. The dynamic properties of the coherent flow structures highly influence the mixing process, therefore, understanding and controlling these structures could prove important in terms of optimizing practical devices in chemical engineering. [43]

POD has already been successfully applied for various chemical process equipment as analyzed, e.g., using two-dimensional (planar) data sets in [80]. Nevertheless, the 2D investigation might have limitations in recovering the entire flow domain. [43]

Doulgerakis et al. [22] investigated the macro-instabilities in a stirred vessel by means of particle image velocimetry (PIV) and proper orthogonal decomposition (POD). In their study, the two dominant frequencies were one-tenth and one-fifth of the impeller rotational speed. The POD technique was also applied for 2D PIV velocity data in [55]. They pointed out the importance of a 3D analysis to improve the understanding of the complex underlying processes. Therefore, a POD analysis is performed in the present work in order to gain the maximum available information.

4.1.2 Macro-instability

The high amplitude flow oscillations having significantly lower frequencies than the blade passage frequency are often termed as macro-instability (MI) oscillations. The investigation of MI in stirred tanks was the subject of numerous studies in the published literature. The flow field was either investigated by measurements (e.g., [34, 33]) or by means of LES computations (e.g., [23]). The

temporal mean flow variations characterized by MIs influence the fluid motion, intensify macro-mixing and, therefore, the overall mixing performance.

Novel analysis methods are introduced for a detailed analysis of the complex three-dimensional turbulent fluid motion in a stirred tank using the single-phase flow of a Newtonian fluid. FFT analysis of the velocity signals has been performed for the entire configuration around the impeller, involving more than one million FFT computations. A four-dimensional POD analysis has been presented considering either the impeller region or the whole stirred tank. The presented methods will be valuable tools in future systematic investigations, where additional effects will be considered, such as different flow properties or Reynolds numbers. The central objective of the present study is to explore various analysis techniques and test their applicability for the investigation of the three-dimensional flow motion in a stirred tank. [43]

4.2 Mathematical Models

Turbulent flow configurations can be investigated using different numerical approaches. Earlier studies applied multiple reference frame or unsteady sliding-mesh RANS models for the description of the hydrodynamics in stirred tanks as reviewed by [48, 49, 76]. Later investigations showed the benefit of LES over RANS methods [19, 32, 61, 67, 85, 86]. Most of these engineering turbulence models have difficulties in accurately predicting the effects of rotation, streamline curvature, and the strong turbulence anisotropy [66, 84], however, they sufficiently characterize the present configuration.

For engineering applications at very high Reynolds numbers, it is very challenging to obtain an appropriate resolution in space and time. In the present case, the impeller Reynolds number $\mathrm{Re} = 10\,800$ is moderate and therefore, a proper resolution can be obtained. The rotation of the zone containing the blades is achieved using the sliding mesh model (SMM) model and the absolute velocity formulation. [43]

4.3 Numerical Details

The computational geometry considered in this work is depicted in Fig. 4.1. The flow is agitated by a three-blade propeller with a diameter of 45 mm. The

internal diameter of the stirred tank is 90 mm. The cylindrical vessel with a non-flat bottom is filled to a height of 97.3 mm. [43]

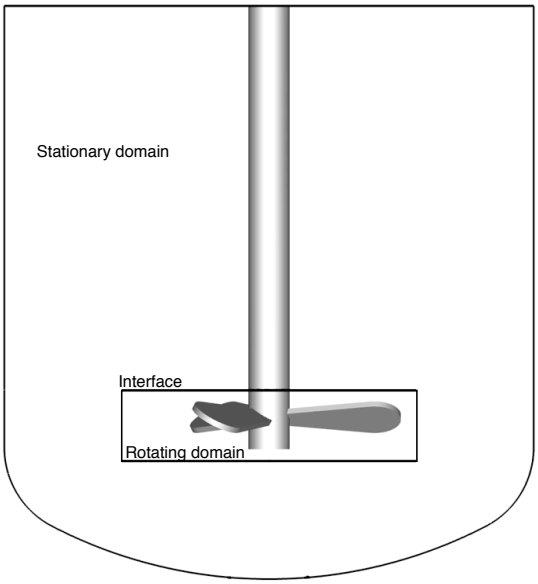

Fig. 4.1: Schematic representation of the stirred tank with a three-blade propeller. The inner rotating and the outer stationary domains are separated by a cylindrical interface. [43]

4.3.1 Computational Mesh

Block-structured grids with hexahedral cells are commonly used for stirred tanks, e.g., for a Rushton turbine, due to the relative simplicity of the geometry. Other types of impellers are often meshed using unstructured tetrahedral elements, even if a large part of the domain remains block-structured using hexahedral cells. Few studies report a fully unstructured mesh in the complete configuration.

The applied computational mesh needed for the finite-volume simulation was generated using the commercial tool ICEM-CFD (Ansys Inc., Canonsburg, PA, USA). The body-fitted, block-structured mesh involves 3 438 182 finite-volume cells (3 339 075 nodes) composed of hexahedral elements using combined O-grid topologies. The block-structure of the inner rotating domain

Table 4.1: The mesh quality in the investigated stirred tank.

Domain	Mesh skewness	Mesh orthogonal quality
outer stationary	0.62	0.59
inner rotating	0.86	0.23

includes 2 181 630 hexahedral cells incorporating the blades, while the stationary outer region is discretized in a slightly coarser manner by 1 049 787 hexahedral cells [43]. The computational mesh used for the present case is depicted in Fig. 4.2. For all the mesh elements, the orthogonal quality is better than 0.23 (1 being the optimum) and the equi-angle skewness is better than 0.86 (1 being the worst and 0 the optimum), leading to a very good mesh quality. The outer stationary domain shows a higher mesh quality than the inner rotating part (Table 4.1), as the block-structured body-fitted mesh generation of the considered geometry with a propeller is challenging compared, e.g., to a Rushton type of impeller. The volume of the smallest grid volume elements is 3.36×10^{-5} mm^3. A very fine resolution was implemented in the vicinity of the walls. The highest wall normal grid distance is 111 μm and 158 μm on the tank and the propeller walls, respectively. This provides a near-wall resolution of less than one in wall units in a majority of the cells. [43]

(a) (b)

Fig. 4.2: Block-structured computational mesh for the investigated stirred tank configuration with (a) the surface mesh of the tank and (b) the surface mesh of the blades and the interface of the inner rotating domain. [43]

An extremely fine resolution is provided at the blades, which has been found to be very important in order to correctly resolve the flow separation. The boundary layer is fully resolved and not modeled in the present work. This direct resolution is hardly possible for very high Reynolds numbers, but is feasible for a moderate Reynolds number as in the present case.

4.3.2 Computational Details of the Flow Simulation

The fluid flow simulation was performed using the commercial finite-volume fluid-flow solver ANSYS Fluent 14 (Ansys Inc., Canonsburg, PA, USA), applying the double-precision pressure-based method. The velocity-pressure coupling was treated by the coupled solver. Zero velocity was applied as an initial condition for the entire domain. No artificial turbulence fluctuations were superimposed on the initial velocity field. Hence, all the unsteady flow features observed are solely the result of stirring by the blades within the considered geometry. [43]

The fluid is represented as isothermal with incompressible Newtonian properties. The constant density and the dynamic viscosity were chosen as $1\,000$ kg/m^3 and as 0.001 Pa $\cdot$ s, respectively.

The convective terms in the momentum equations were discretized with a second-order central differencing scheme, while a second-order scheme was chosen for the pressure interpolation scheme. The Least Squares cell-based approach was employed for the interpolation of variables on the cell faces. The time advancement was realized using an implicit second-order scheme. A constant time step of 0.001 s ensured that the CFL number is less than unity everywhere in the computational domain. [43]

A symmetry boundary condition was implemented at the top of the computational domain. A standard, no-slip boundary condition was employed along the walls. The speed of the rotation was chosen as 80 rpm (1.333 rps) in the clockwise direction – pumping down – for the sliding mesh model (SMM) computations. This corresponds to an impeller Reynolds number of $\mathrm{Re} = ND^2\rho/\mu = 10\,800$, and $v_{tip} = \omega\frac{D}{2} \approx 0.38$ m/s. [43]

Before starting the POD procedure, 28 revolutions were performed, corresponding to $21\,000$ time steps. One time step generally converged in 15 iterations and the velocity residuals were lower than the tolerance of 10^{-6}.

In the computation of the last four revolutions, all velocity values were stored in the entire 3D domain for further analysis at every other time step.

This corresponds to a sampling frequency of 500 Hz leading to 1500 3D snapshots. [43]

Computations were carried out in parallel using 16 computing cores on a workstation equipped with 64 GB of memory and an Intel Xeon 64-bit Processor E5-2687 W having a 3.1 GHz clock rate using HyperThreading technology. For the mesh considered in this study, around 18 GB of computer memory were required for the simulation. The complete numerical simulations were completed in approximately 567 hours wall-clock-time, corresponding to almost 24 days on 16 computing cores in parallel. [43]

4.3.3 Computational Details of the POD Analysis

Proper orthogonal decomposition (POD) was used in this work to study the characteristic flow features in a stirred reactor tank. The first mode – sometimes denoted as zeroth mode – of the POD analysis provides the temporal mean of the investigated variable. The POD analysis was performed on the complete three-dimensional domain involving all 3 velocity components in every finite volume cell. The obtained modes were also analyzed as vector variables having 3 scalar components, similar to the original velocity vector field. [43]

The POD decomposition was performed in two different regions: in the outer stationary zone and in the rotating zone around the propeller, separated by a cylindrical interface.

The stationary region contains the larger portion of the whole tank surrounding the propeller. Most of the turbulent structures were expected to lie within this domain. All of the computational finite volume cells were directly included in the POD examination of this outer region, providing more than one million 3D vector variables. In this outer stationary region, the absolute velocities were considered [43].

In order to investigate the flow structures close to the propeller, a second domain incorporating the propeller was studied. This inner zone rotates with the speed specified in the LES computation using the sliding mesh model (SMM). In this analysis, the relative flow velocities were taken into consideration. The very fine mesh resolution in this region involved over 2.1 million computational cells. All of these cells were directly involved in the POD analysis without down-sampling the original mesh to a lower spatial resolution. [43]

4.4 Results and Discussion

4.4.1 Flow Field

An instantaneous velocity field is shown in Fig. 4.3 using the surface-projected (in-plane) streamtraces in a given time step.

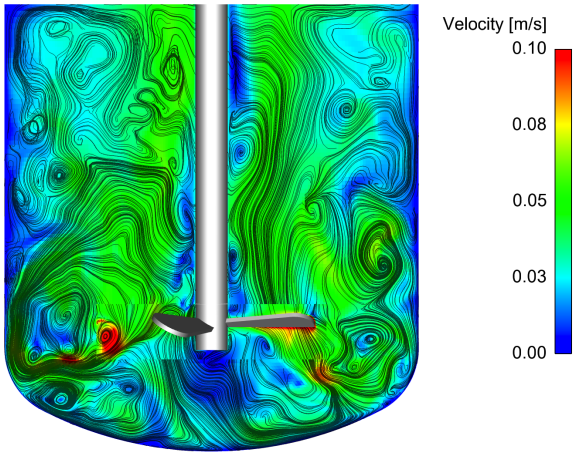

Fig. 4.3: Contour-plot representation of the instantaneous velocity magnitude over the entire cross section in the middle of the tank. Two-dimensional surface-projected (in-plane) streamtraces depict the complex flow structures. [43]

The rotating frame from the sliding mesh computation rotates with the same speed as the propeller of the stirred tank. Accordingly, the relative velocities in the rotating region are considered relative to the moving frame.

According to [47], the vortex can be characterized by the eigenvalues of the tensor $\left(S^2 + \Omega^2\right)$, where S represents the symmetric part and Ω denotes the anti-symmetric part of the velocity gradient tensor. They define the flow vortex core with the negative second eigenvalue of the tensor $\left(S^2 + \Omega^2\right)$, the so-called λ_2-criteria.

Trailing-edge vortex structures are visualized by the iso-surface of the λ_2-criteria. The formation of the trailing vortex is revealed in the wake of the propeller blades. The movement of vortices shows a downward direction. Precessing vortices near the rotating shaft are revealed, where these vortical structures spread upwards and thus enhance the mixing. [43]

Exemplary instantaneous iso-surface of the λ_2-criterion for $\lambda_2 = 600\ \mathrm{s}^{-2}$ is shown in Fig. 4.4. The topology of this quantity reveals the existence of strong coherent structures in the considered flow. It illustrates qualitatively the complexity of the turbulent structures induced by rotating the blades.

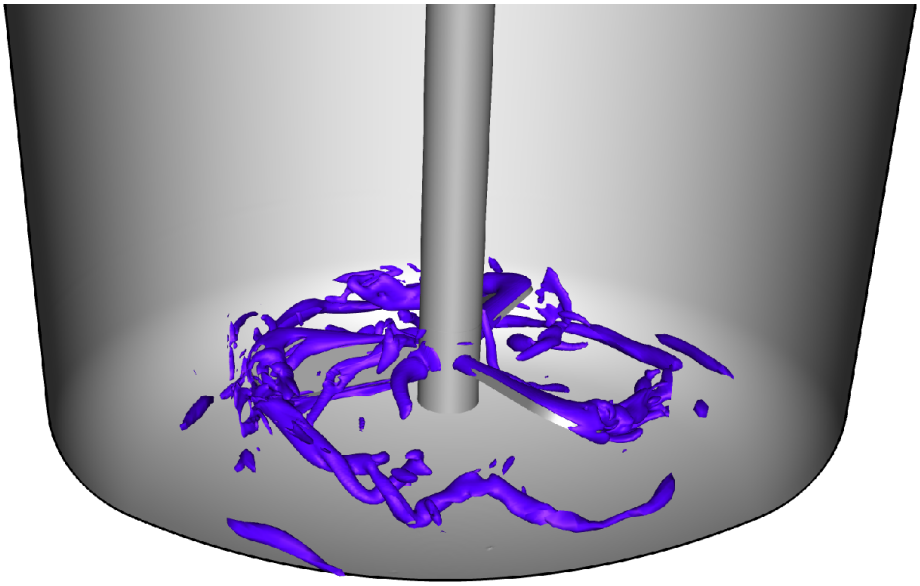

Fig. 4.4: λ_2-criterion in the considered flow configuration. [43]

4.4.2 Results of the POD Analysis

Considering the POD modes as three-dimensional vector variables, they can be illustrated using vectors (glyphs) as well as using a pseudo-streamline representation. The vectors allow for the visualization of both the magnitude as well as the direction in a given location. However, the pseudo-streamlines integrated from the modes – similar to streamlines computed from a velocity field – might better demonstrate the complex three-dimensional structures of a given POD mode.

A single visualization of the obtained three-dimensional modes is challenging; different representations on the first three modes are applied (see Figs. 4.7-4.9) in order to appreciate the three-dimensional results. The POD modes are shown using vectors in Fig. 4.8, and by the line integral convolution (LIC)

technique in Fig. 4.9 for the rotating reference frame at three horizontal cut-planes: above the propeller, in the height of the propeller, and below it. It should be kept in mind that the magnitudes of the various modes are very different, as the modes are scaled individually to allow for a meaningful representation. Therefore, they are not intended to compare the different modes with one another. [43]

The first mode – corresponding to the temporal average – is strongly influenced by the propeller. The circular radial structure is well visible and the direction is opposite that of the propeller movement.

The second mode shows a strong radial flow direction. This mode can be considered as the secondary flow of the system. The flow features reveal a mostly straight direction in this mode.

The third mode obtained from the relative velocities illustrates two major flow directions. Additionally, in the horizontal cut-planes, the modes represent a spiral-like structure. Below the propeller, this mode approaches the inside of the domain, while above the propeller the directions differ, appearing outside of the rotating frame. On the other hand, the vertical cut-planes reveal a second flow direction of the third mode: changing the directions at the height of the propeller.

The coherent flow structures – identified here by the first three modes – in the inner rotating domain are depicted in Figs. 4.7(a)-4.7(c). These figures exemplify how the POD analysis can separate the main flow features in a complex dynamic system. [43]

The analysis of the second and the third modes seems particularly helpful to understand the mixing phenomena in a stirred tank as exemplified, e.g., by showing the trailing-edge vortices represented by these two modes in Figs. 4.7(n)-4.7(o). It allows for the efficient use of this method for the further optimization of a given system.

Next, the complex flow is further investigated in a quantitative manner using POD. Over 98% of the overall energy is contained within the first 21 modes in the outer stationary domain. Due to the fact that the remaining modes would not significantly affect the results, only these 21 modes are involved in all the presented analysis for this region. [43]

The energy contribution of the modes in the stationary outer domain is depicted in Fig. 4.5 and given in Table 4.2. The second mode onwards each contribute less then 3% of the energy (Fig. 4.5(b)). Five modes are sufficient to capture 90% of the total kinetic energy and 11 modes are needed for 95%. The first 21 modes capture 98% of the total kinetic energy and are used for the further analysis. [43]

Table 4.2: Energy contribution of the first four POD modes.

Modes	Inner rotating domain	Outer stationary domain
1	91.71%	81.7%
2	4.92%	2.75%
3	1.41%	2.49%
4	0.08%	1.89%

A similar POD analysis can be performed replacing the three-dimensional velocity vectors by the three-dimensional vorticity vectors. The energy contribution based on the vorticity analysis in the same stationary domain around the propeller is represented in Fig. 4.6. Here, the first mode is far from as dominant as for the velocity POD-analysis. In order to once again capture of 98% of the total energy, 112 modes should be included. [43]

The selection of both velocity and vorticity was initially motivated in this study by the goal of comparing both approaches. However, the analysis relying on the vorticity vectors does not shown any real benefit compared to a direct analysis of the 3D velocity components. Since vorticity is an indirect quantity, thus prone to larger uncertainties, it is recommended to stick to POD of 3D velocity fields in the future. [43]

In the inner rotating domain, the energy contribution of the first four modes based on the relative velocities are given in Table 4.2. The first mode – the temporal mean relative velocity – captures alone more than 90% of the total kinetic energy. The first 3 modes – much less than in the outer domain – capture more than 98% of the total kinetic energy and are used for the further investigations. [43]

4.4.3 Quantification of Macro-instability

The macro-instability oscillations are investigated using more than one million FFT analyses considering the temporal velocity signals in the outer stationary region of the stirred tank.

The local characteristic frequencies are extracted in every single finite volume computational cell. This allows for a scalar field to be built based on the these frequency values for this region. This characteristic frequency distribution is portrayed in Fig. 4.10 using different cut-planes. This figure shows very

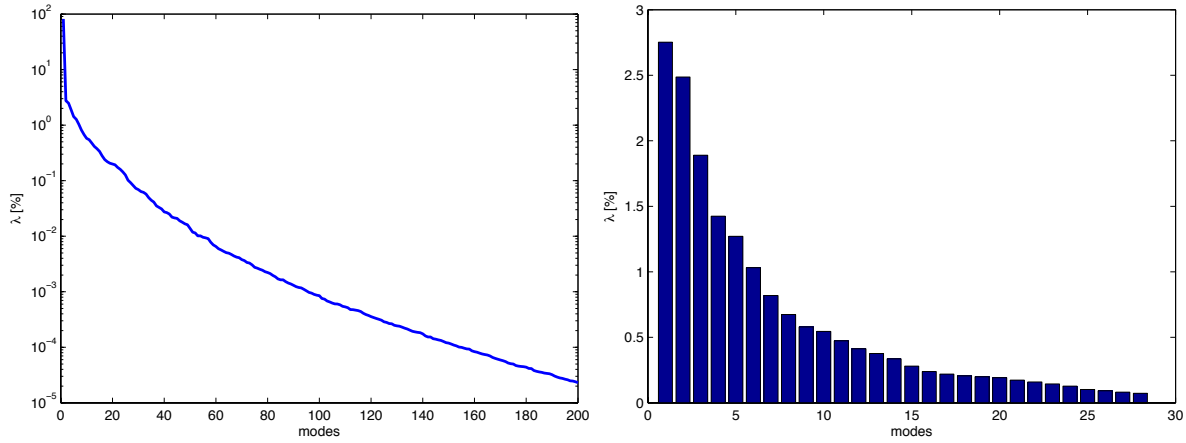

(a) Semi-logarithmic plot of modes from 1 to 200

(b) Modes from 2 to 29

Fig. 4.5: Energy contribution of the modes based on the velocity POD analysis in the stationary outer domain: (a) The first 200 modes and (b) modes 2 to 29. [43]

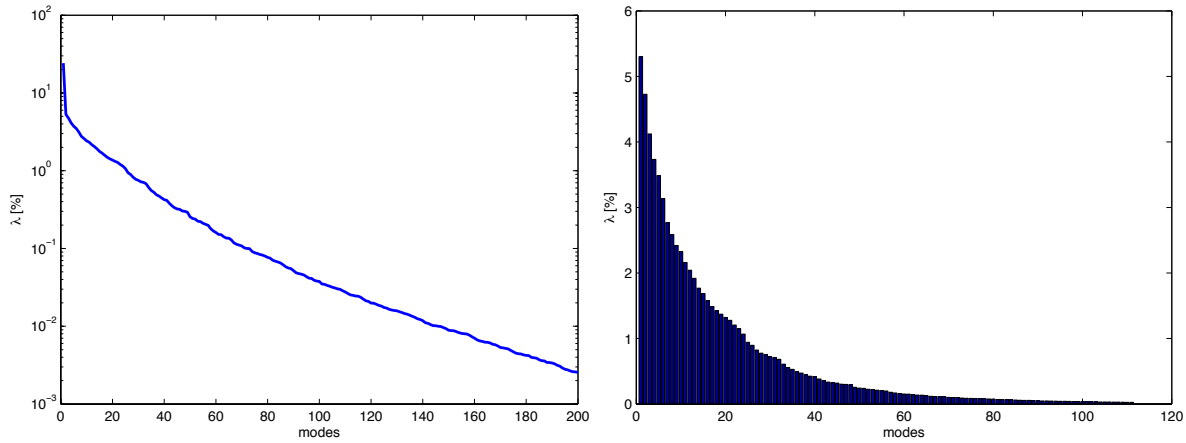

(a) Semi-logarithmic plot of modes from 1 to 200

(b) Modes from 2 to 112

Fig. 4.6: Energy contribution of the modes based on the vorticity POD analysis in the stationary outer domain. (a) The first 200 modes and (b) modes 2 to 112. [43]

well that these values are not fully homogenous in the considered geometry. If the frequency values would be only dominated by the blade passage frequency, a constant frequency of roughly 4.0 Hz should be obtained in every compu-

Table 4.3: FFT analysis in the outer stationary region based on velocity values in the last 4 revolutions.

Frequency	Fraction
0.49 Hz	38.8%
0.73 Hz	28.4%
0.98 Hz	14.0%

tational cell. However, this figure clearly shows that the dominant frequency value is not homogenous in the considered geometry. The local variations of this quantity underline the complexity of the present turbulent flow configuration. The obtained frequency values range from 0.49 Hz to 4.80 Hz (one order of magnitude), and are in general lower than the frequency corresponding to the rotational movement of the propeller blades. The blade passage frequency dominates only in the immediate vicinity of the stirrer. The most dominant frequency in the outer region is about one-eighth of the blade passage frequency, and corresponds to the motion of large-scale vortical structures. It must be kept in mind that the obtained frequency distribution is specific to the investigated geometry and process conditions. Comparable studies involving Rushton turbines mention typically a factor 10 between dominant frequency and the rotation frequency (see, e.g., [62]). Systematic studies will be necessary to clarify the dependence between dominant frequency, blade passage frequency, and Reynolds or power number. [43]

Due to the variations in the finite volume cell sizes, the occurrence of the local maximum frequency values are evaluated using volume-averaging as shown in Fig. 4.11. The smallest frequency resolved in this study corresponds to 0.24 Hz. Higher sampling rate and more snapshots could further improve the frequency resolution. Nevertheless, the present resolution appears to be acceptable, since this smallest frequency of 0.24 Hz does not appear in the presented analysis. The frequencies 0.49 Hz, 0.73 Hz, and 0.98 Hz dominate in more than 81% of the outer stationary domain as summarized in Table 4.3. The characteristic frequency of 0.49 Hz can be found in 38.8% of this region in the stirrer geometry. The second most common frequency of 0.73 Hz is responsible for 28.4% of the present configuration. The dominant frequencies correspond to around one-eighth and one-fifth of the blade passage frequency for the present configuration [43].

Table 4.4: FFT analysis in the outer stationary region based on the POD time-coefficients.

Time-coefficients	Frequency based on velocity	Frequency based on vorticity
1	0.49 Hz	0.49 Hz
2	0.49 Hz	0.49 Hz
3	0.73 Hz	0.73 Hz
4	0.73 Hz	0.73 Hz

4.4.4 POD Analysis of the Velocity Modes

The temporal coefficients of the POD analysis can be further investigated by FFT.

The FFT analysis in the outer domain of the POD time-coefficients yields the characteristic frequency of 0.49 Hz for the first and second time-coefficients, while 0.73 Hz results for the third and fourth coefficients. If the vorticity is applied in the 3D-SPOD analysis instead of the absolute flow velocity, the same frequencies are obtained for these four time-coefficients as summarized in Table 4.4. The same values are obtained as in the previous Subsection 4.4.3, so both the FFT analysis of the individual computational cells as well as the FFT of the POD time-coefficients suggest the characteristic frequencies of 0.49 Hz and 0.73 Hz, i.e., with dimensionless frequencies $f' = f/N = 0.37$ and $f' = 0.55$, respectively. Although the present configuration is different from the Rushton turbine studied by [69], it is interesting to note, that the here obtained first non-dimensional frequency is half of their values. [43]

In the inner domain, the FFT analysis of the POD time-coefficients based on the relative velocity – where the system is rotating with the blades – shows a slightly different picture (Table 4.5). Here, a characteristic frequency value of 1.465 Hz results for the first three time-coefficients. This corresponds to the three main modes representing over 98% of the total kinetic energy. This value is exactly twice as large as that for the third and fourth coefficients in the stationary region, see Table 4.4. [43]

Table 4.5: FFT analysis in the inner rotating region based on the POD time-coefficients.

Time-coefficients	Frequency based on velocity
1	1.465 Hz
2	1.465 Hz
3	1.465 Hz

4.4.5 Phase Portraits

Phase portrait diagrams can elucidate the relationship between the time-coefficients of two modes, representing the two-dimensional projection of the phase portrait into a plane. Characteristic shapes, such as a circle or an ellipse, can reveal periodic flow structures. The circular shape depicted in Fig. 4.12(b) illustrates cyclic variations of modes 1 and 2. A similar interaction process can be observed for modes 2 and 3 in Fig. 4.12(c). Liné et al. [55] have shown circular results for modes 2 and 3 as well, based on their two-dimensional measured velocity data in a mixing tank with a Rushton turbine. The phase portraits for the present three-dimensional computation demonstrate periodic coupling between these mode pairs, where the phases are shifted by a quarter period. It reveals an organized flow motion in the inner rotating region, as obtained from the relative flow velocities. [43]

4.5 Conclusion

The purpose of the present chapter was to investigate the complex hydrodynamics in a stirred tank. The numerical computations relied on a large eddy simulation. The coherent flow structures of the complex three-dimensional turbulent hydrodynamics have been successfully extracted using the 3D Snapshot POD method. The POD analysis has been performed in two parts. First, the hydrodynamics in a stirred tank was investigated considering a stationary domain in order to characterize the global mixing in the tank. In a subsequent step, a smaller domain – the rotating reference frame enclosing the propeller blades – was analyzed. In the latter case, the flow velocities considered lie in a relative coordinate-system. This second analysis might deliver a deeper insight into the blade design reducing the local flow effects, such as the trailing-

edge vortices. The dynamics of the main flow structures have been successfully reconstructed using 3 modes corresponding to over 98% of the total kinetic energy in the inner rotating domain and using 21 modes in the outer stationary region. [43]

The blade passage frequency is 4.0 Hz in the present configuration. It can be expected that this frequency is dominating the flow in the vicinity of the stirrer. However, different analysis techniques used in the present study showed that one-eighth and one-fifth of the blade passage frequency are dominating the outer flow field. These lower frequencies characterizing the large-scale flow motions are termed macro-instability (MI) in the scientific literature. They have been studied by many groups (see e.g. [34, 69, 62]) because it is believed that they play a crucial role concerning mixing. [43]

All the previous studies on macro-instability in stirred tank reactors considered measurements either at single points or in two-dimensional cut-planes. To the best knowledge of the author, the present author [43] considered first the entire three-dimensional information for such an investigation. Due to the complexity of these systems, it is expected that the underlying phenomena can only be examined in every details if the three-dimensional structures are considered. It is well-known that the dynamic properties of the investigated coherent flow structures highly influence the mixing process. Therefore, understanding and controlling these structures could prove important in terms of optimizing practical devices in chemical engineering. It is believed that the detailed understanding of the hydrodynamics is essential in order to further improve the mixing, hence the product quality.

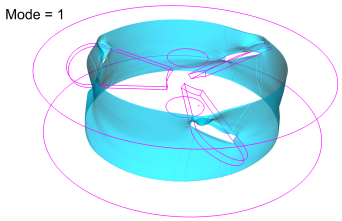

(a) Isosurface of mode 1

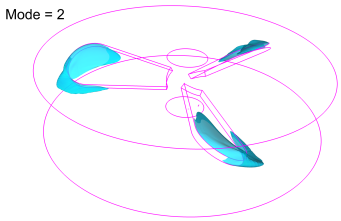

(b) Isosurface of mode 2

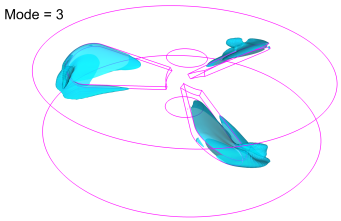

(c) Isosurface of mode 3

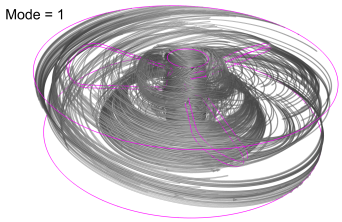

(d) Pseudo-streamlines of mode 1

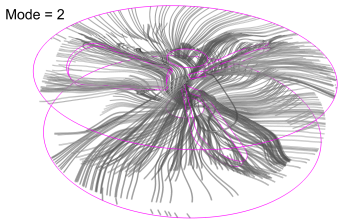

(e) Pseudo-streamlines of mode 2

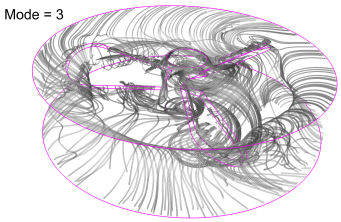

(f) Pseudo-streamlines of mode 3

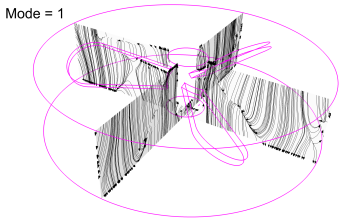

(g) Surface-projected pseudo-streamlines of mode 1

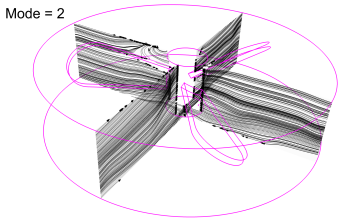

(h) Surface-projected pseudo-streamlines of mode 2

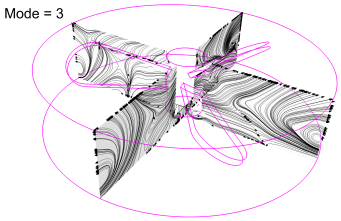

(i) Surface-projected pseudo-streamlines of mode 3

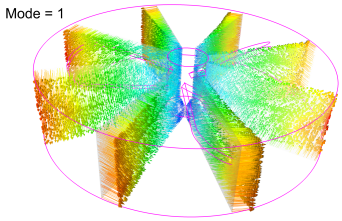

(j) Vectors of mode 1

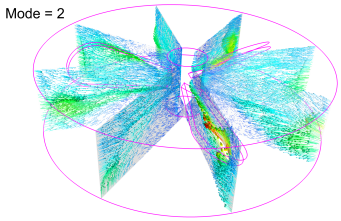

(k) Vectors of mode 2

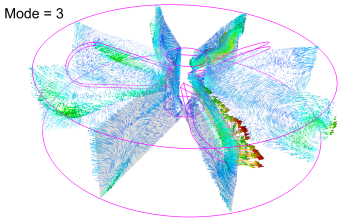

(l) Vectors of mode 3

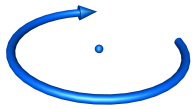

(m) Direction of the propeller rotation

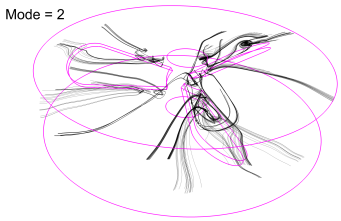

(n) Trailing-edge vortices originating from propeller blade obtained from mode 2

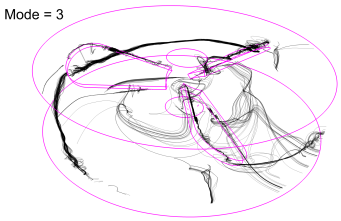

(o) Trailing-edge vortices originating from propeller blade obtained from mode 3

Fig. 4.7: Visualization of the coherent flow structures represented by the first three modes in the rotating frame. [43]

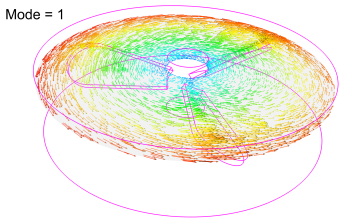

(a) Vectors of mode 1 above the propeller.

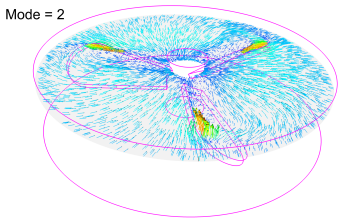

(b) Vectors of mode 2 above the propeller.

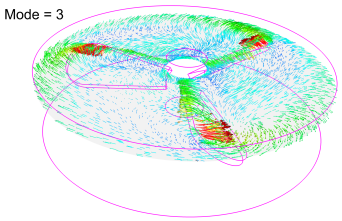

(c) Vectors of mode 3 above the propeller.

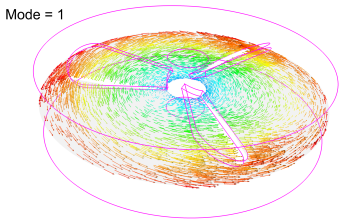

(d) Vectors of mode 1 at the height of the propeller.

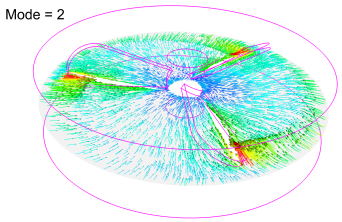

(e) Vectors of mode 2 at the height of the propeller.

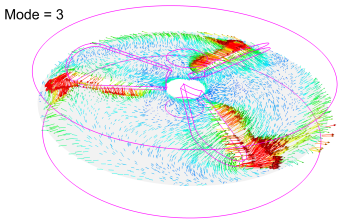

(f) Vectors of mode 3 at the height of the propeller.

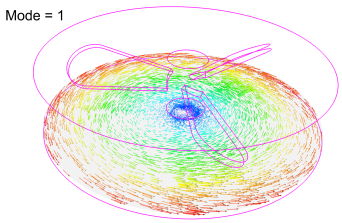

(g) Vectors of mode 1 below the propeller.

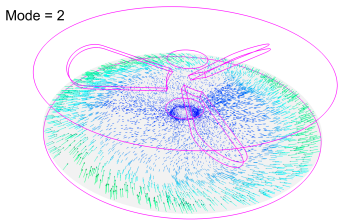

(h) Vectors of mode 2 below the propeller.

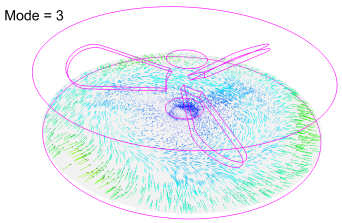

(i) Vectors of mode 3 below the propeller.

Fig. 4.8: Vector representation of the coherent flow structures represented by modes 1, 2, and 3 in the rotating frame. [43]

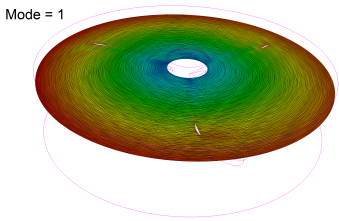

(a) Surface-projected pseudo-streamlines of mode 1 above the propeller.

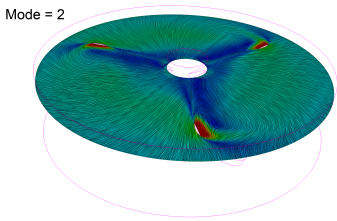

(b) Surface-projected pseudo-streamlines of mode 2 above the propeller.

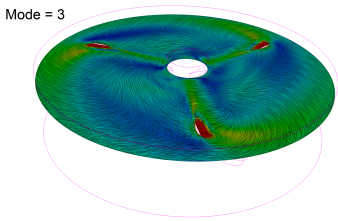

(c) Surface-projected streamlines of mode 3 above the propeller.

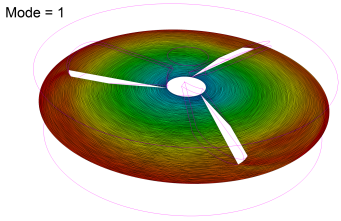

(d) Surface-projected pseudo-streamlines of mode 1 at the height of the propeller.

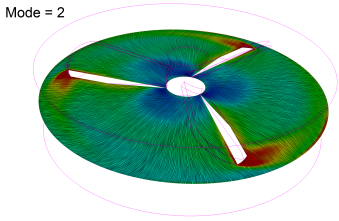

(e) Surface-projected pseudo-streamlines of mode 2 at the height of the propeller.

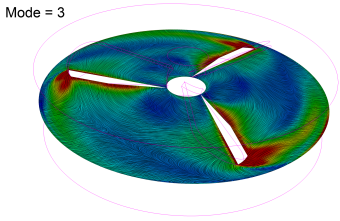

(f) Surface-projected pseudo-streamlines of mode 3 at the height of the propeller.

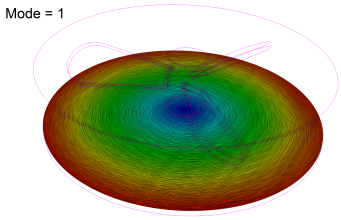

(g) Surface-projected pseudo-streamlines of mode 1 below the propeller.

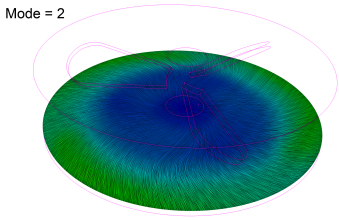

(h) Surface-projected pseudo-streamlines of mode 2 below the propeller.

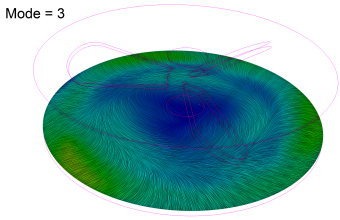

(i) Surface-projected pseudo-streamlines of mode 3 below the propeller.

Fig. 4.9: Line integral convolution (LIC) visualization of the coherent flow structures for modes 1, 2, and 3 in the rotating frame. [43]

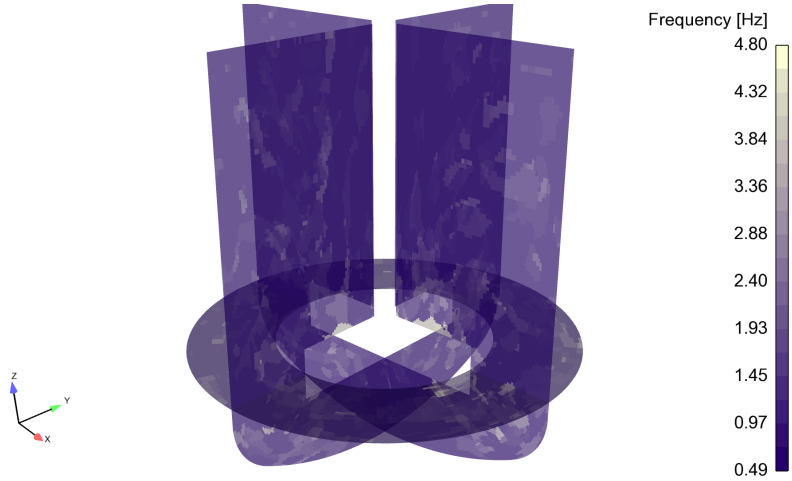

Fig. 4.10: The local characteristic frequencies in the outer stationary domain. [43]

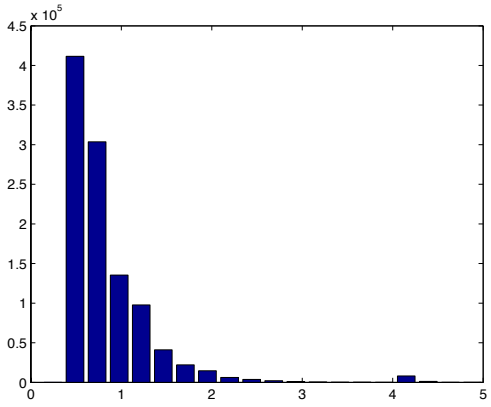

Fig. 4.11: Histogram of the local characteristic frequencies shown in Fig. 4.10. [43]

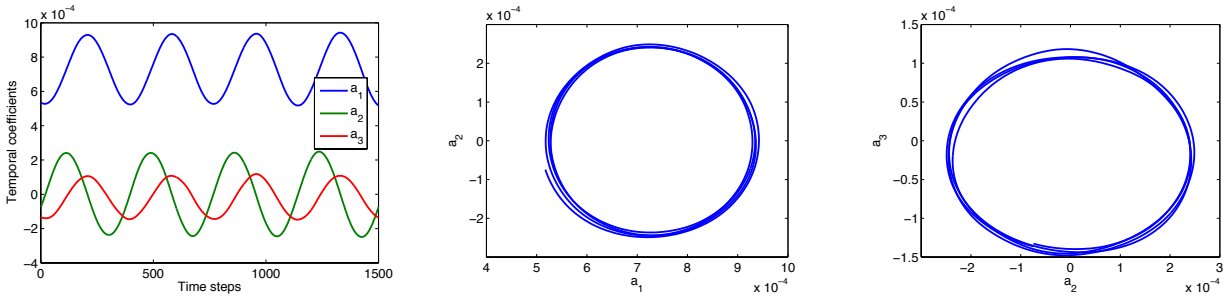

Fig. 4.12: Temporal evolution of the velocity POD modes obtained over 4 revolutions in the inner rotating region. [43]

Chapter 5

Direct Numerical Simulation

The most exact numerical description of a turbulent flow field is achieved using the so-called direct numerical simulation (DNS) approach, for which the Navier-Stokes equations are solved as exactly as possible on an extremely fine grid: DNS results are often called "numerical experiments". Nowadays, DNS is only possible for simple configurations and low-Reynolds number flows even on large computing clusters, because this type of simulation requires enormous computational resources. Furthermore, DNS is associated with complex post-processing and visualization issues, due to the extremely large quantity of raw data delivered by such computations. Nevertheless, DNS has become an essential and well-established research tool to investigate the structure of turbulent flames, since they do not rely on any approximate turbulence models [36].

Using a realistic description of chemistry on a growing number of grid elements rapidly leads to a huge discretized equation system and to an enormous computation time. In this case parallel computations are absolutely necessary. The simulation time can be highly reduced by dividing the numerical domain into smaller sub-domains (a method called Domain Decomposition). Each processor of the parallel supercomputer is then responsible for its own sub-domain and exchanges information with its topological neighbors. The inter-processor communication relies on the Message-Passing Interface (MPI) communication library.

5.1 Introduction

The ignition and initial development of a flame inside a turbulent flow is a problem of great interest, both from a fundamental (complex, multi-scale, fully coupled physical process) and from a practical (internal combustion engines, gas turbines re-ignition, security issues, etc.) point of view. In recent years, numerical studies have become increasingly useful to understand such complex processes. In particular, Direct Numerical Simulations (DNS) have been known for over 20 years now to be ideally suited to investigate turbulent flames [15, 64], because they do not require any particular assumption concerning the turbulence. Nevertheless, due to the huge cost of DNS, strong hypotheses have often been introduced to reduce the requested computing times [64].

When considering quantitative problems like predictions of intermediate radicals, pollutant emissions, or ignition/extinction limits, the reaction processes should normally be described using complete chemical models [36]. In the past, such computations relying on detailed models have been limited to two dimensions due to the huge numerical cost associated with three-dimensional DNS. But, of course, turbulence is fundamentally a three-dimensional process, so that two-dimensional simulations necessarily have a questionable validity and generality. This explains why several research groups are now focusing their efforts on three-dimensional DNS including a realistic description of the chemical reactions, as shown here.

The presented results illustrate three-dimensional direct simulations of turbulent reacting flows.

5.2 Direct Numerical Simulations

The DNS approach consists in solving exactly all the physical space and time scales embedded in the representative flow equations, without any assumed model for turbulence. A DNS must thus provide an exact solution for both fluid dynamics and flame structure. Even though this method requires prohibitive numerical costs for practical configurations, it offers an excellent complement to experiments in order to assess the importance of various physical mechanisms, to obtain complementary information on flame structure, and therefore to improve turbulent combustion modeling (see e.g. [21, 35] and references therein). In fact, the rapid growth of computational capabilities has presented significant opportunities for the DNS of turbulent combustion: offering pos-

sibilities to achieve higher Reynolds numbers, a larger sample of turbulent structures for better statistical analysis, a more complete temporal development of the turbulent flame and the simulation of fuels with higher chemical complexity.

5.2.1 Numerics

The DNS code employed in this work is the massively parallel flame solver, *Parcomb3D* [52, 81], which solves the full compressible reactive Navier-Stokes system coupled with detailed chemistry and multicomponent transport models. These governing equations are solved on a conventional equidistant three-dimensional Cartesian grid with high-order numerical schemes. A spatial sixth-order central scheme, progressively reduced to a one-sided fourth-order near the boundaries is used for spatial discretization. The improved skew-symmetric formulation [40] has been implemented for the convective terms in order to reduce even further numerical dissipation and increase stability.

According to this scheme, the derivative of a general convective term can be written as:

$$\frac{\partial(\rho a u_j)}{\partial x_j} = \frac{1}{2}\frac{\partial(\rho a u_j)}{\partial x_j} + \frac{1}{2}\frac{\partial(\rho u_j)}{\partial x_j} + \frac{\rho u_j}{2}\frac{\partial a}{\partial x_j} \quad . \tag{5.1}$$

Time integration is performed in an explicit manner with a fourth-order Runge-Kutta scheme. The extended Navier-Stokes Characteristic Boundary Conditions (NSCBC, [10, 65]) are used, with non-reflecting boundaries and pressure relaxation applied along all open faces.

Parcomb3D is parallelized using a three-dimensional domain decomposition and MPI message passing, offering a 14% single-core peak performance and a near perfect parallel scaling for a full three-dimensional run using 4 096 computing cores on the *IBM BlueGene/P*. Further generic details concerning code structure, optimization and application can be found for instance in [37].

5.2.2 Finite Difference Discretization Scheme

The computation of finite differences of order of six [53] (third-order at the boundaries) is particularly important in direct numerical simulations. The

mesh can be equidistant or non-equidistant in space. The first and second derivatives are evaluated using the following relationships as summarized in [52]:

$$\frac{\partial f}{\partial x} = \frac{\partial f}{\partial \xi}\frac{\partial \xi}{\partial x} \quad . \tag{5.2}$$

The second order derivative can be written in the same manner:

$$\frac{\partial^2 f}{\partial x^2} = \frac{\partial^2 f}{\partial \xi^2}\left[\frac{\partial \xi}{\partial x}\right]^2 - \frac{\partial f}{\partial \xi}\frac{\frac{\partial^2 x}{\partial \xi^2}\frac{\partial \xi}{\partial x}}{\left[\frac{\partial x}{\partial \xi}\right]^2} \quad . \tag{5.3}$$

The expression for first order derivative can be formulated in the core (inner) part of the domain:

$$\frac{\partial f}{\partial \xi} = \frac{(f_{i+3} - f_{i-3}) + 9\,(f_{i-2} - f_{i+2}) + 45\,(f_{i+1} - f_{i-1})}{60} \quad . \tag{5.4}$$

At the left boundary, we get:

$$\frac{\partial f}{\partial \xi} = \frac{2\,(f_{i+3} - f_{i+2}) + 7\,(f_{i+1} - f_{i+2}) + 11\,(f_{i+1} - f_i)}{6} \tag{5.5}$$

$$\frac{\partial f}{\partial \xi} = \frac{(f_{i+4} - f_i) + 2\,(f_{i+2} - f_i) + 6\,(f_{i+2} - f_{i+3}) + 10\,(f_{i+2} - f_{i+1})}{12} \tag{5.6}$$

$$\begin{aligned}\frac{\partial f}{\partial \xi} = \Big[&2\,(f_{i+5} - f_{i+4}) + 3\,(f_i - f_{i+1}) + 13\,(f_{i+3} - f_{i+4}) \\ &+ 20\,(f_{i+3} - f_{i+2}) + 27\,(f_{i+3} - f_{i+1})\Big] / 60\end{aligned} \tag{5.7}$$

while the right boundary is expressed as:

$$\begin{aligned}\frac{\partial f}{\partial \xi} = -\Big[&2\,(f_{i-5} - f_{i-4}) + 3\,(f_i - f_{i-1}) + 13\,(f_{i-3} - f_{i-4}) \\ &+ 20\,(f_{i-3} - f_{i-2}) + 27\,(f_{i-3} - f_{i-1})\Big] / 60\end{aligned} \tag{5.8}$$

$$\frac{\partial f}{\partial \xi} = -\frac{(f_{i-4} - f_i) + 2\,(f_{i-2} - f_i) + 6\,(f_{i-2} - f_{i-3}) + 10\,(f_{i-2} - f_{i-1})}{12} \tag{5.9}$$

$$\frac{\partial f}{\partial \xi} = -\frac{2\,(f_{i-3} - f_{i-2}) + 7\,(f_{i-1} - f_{i-2}) + 11\,(f_{i-1} - f_i)}{6} \quad . \tag{5.10}$$

Derivatives of $\partial\xi/\partial x$ appeared Eq. (5.2) can also be evaluated using the above presented finite difference schemes.

The second derivative in the domain is expressed as:

$$\frac{\partial^2 f}{\partial \xi^2} = \Big[2\left(f_{i-3} - f_{i-2}\right) + \left(f_{i+3} - f_{i+4}\right) + 25\left(f_{i-1} - f_{i-2}\right) + \left(f_{i+1} - f_{i+2}\right) + 245\left(f_{i-1} - f_i\right) + \left(f_{i+1} - f_i\right)\Big] / 180 \quad . \tag{5.11}$$

The second order derivative at the left boundary is written as:

$$\frac{\partial^2 f}{\partial \xi^2} = \left(f_{i+2} - f_{i+3}\right) + 2\left(f_i - f_{i+1}\right) + 3\left(f_{i+2} - f_{i+1}\right) \tag{5.12}$$

$$\frac{\partial^2 f}{\partial \xi^2} = \frac{\left(f_{i+3} - f_{i+4}\right) + 3\left(f_{i+3} - f_{i+1}\right) + 6\left(f_{i+2} - f_{i+1}\right) + 11\left(f_i - f_{i+1}\right)}{12} \tag{5.13}$$

$$\frac{\partial^2 f}{\partial \xi^2} = \frac{\left(f_{i+1} - f_i\right) + \left(f_{i+3} - f_{i+4}\right) + 15\left(f_{i+1} - f_{i+2}\right) + \left(f_{i+3} - f_{i+2}\right)}{12} \tag{5.14}$$

similarly, the second order derivative at the right boundary is given by:

$$\frac{\partial^2 f}{\partial \xi^2} = -\frac{\left(f_{i-1} - f_i\right) + \left(f_{i-3} - f_{i-4}\right) + 15\left(f_{i-1} - f_{i-2}\right) + \left(f_{i-3} - f_{i-2}\right)}{12} \tag{5.15}$$

$$\frac{\partial^2 f}{\partial \xi^2} = -\frac{\left(f_{i-3} - f_{i-4}\right) + 3\left(f_{i-3} - f_{i-1}\right) + 6\left(f_{i-2} - f_{i-1}\right) + 11\left(f_i - f_{i-1}\right)}{12} \tag{5.16}$$

$$\frac{\partial^2 f}{\partial \xi^2} = \left(f_{i-2} - f_{i-3}\right) + 2\left(f_i - f_{i-1}\right) + 3\left(f_{i-2} - f_{i-1}\right) \quad . \tag{5.17}$$

The derivatives of $\partial^2\xi/\partial x^2$ appeared in Eq. (5.3) are also evaluated using the above presented finite difference schemes. An identical approach can be deduced for directions y and z.

5.3 Computational Details

Direct Numerical Simulations (DNS) have been conducted to study the response of initially laminar spherical premixed methane-air flame kernels to successively higher turbulence intensities at five different equivalence ratios.

The numerical experiments include a 16-species/25-step skeletal mechanism for methane oxidation and a multicomponent molecular transport model. Highly turbulent conditions (with integral Reynolds numbers up to 4 513) have been accessed and the effect of turbulence on the physical structure of the flame, in particular the consumption speed S_c (suitably scaled to quantify the turbulent flame speed S_T), has been investigated [29, 28].

Initially perfectly spherical laminar premixed methane–air flames are considered in all computations, within a cubic computational domain of sides $L = 4.0$ cm (Fig. 5.1) and a uniform grid spacing of 20 – 35 μm for the mild to the most intense turbulent cases, respectively, ensuring the full resolution of the smallest (Kolmogorov) scales, since their length decreases with increasing Re_t. The three-dimensional computation shown in Fig. 5.1 has been realized on a grid with $400 \times 400 \times 400$ finite difference nodes. The turbulent Reynolds number Re_t is 1 400 and u' is 5 m/s. It has been shown [25, 26, 68] that the reaction zone is broad, if not completely homogeneous, making it possible to relax the constrains on the spatial resolution of the reaction zones, since there are no steep flame fronts [83]. The resolution is then purely dictated by the turbulent scales. The ignition and subsequent expansion/development of a premixed flame-kernel under the influence of a turbulent flow field is an excellent configuration, which allows turbulent flames to be studied well away from the influence of external perturbations such as walls and artificial boundary conditions. From a fundamental point of view, it offers the possibility to study highly complex multi-scale flows involving fully coupled physical processes. Simultaneously, it has direct practical relevance in a number of industrial cases including spark-ignition internal combustion engine and gas turbine re-ignition, as well as safety issues.

Methane oxidation is modeled by a 25-step skeletal scheme [12, 75], comprised of 4 elements (H, C, O, N), 16 chemical species (CH_4, O_2, H_2, H_2O, CH_2O, CO, CO_2, HO_2, OH, H, O, CH_3, HCO, H_2O_2, CH_3O, N_2) and 50 elementary reactions (Appendix A). This reaction mechanism is retained here due to its simplicity compared to a full methane oxidation mechanism like the GRI-MECH [13] and provides sufficiently accurate results for lean up to stoichiometric conditions. It has been successfully used for large scale direct simulations of two-dimensional non-premixed methane jet flames [41] and most recently, highly turbulent premixed flames [26, 25]. However, it would be inadequate for methane–rich flames due to the absence of C_2 and higher carbon-chain reactions, the reason why $\Phi \leq 1.0$ for the present study.

The initial mixture composition (Y_i), prescribed burnt (T_b) and unburned (T_u) temperatures, laminar flame speed s_L, thermal flame thickness $\delta_{th} = (T_b - T_u)/\max|\nabla T|$ and a Karlovitz number estimate $\mathrm{Ka} \approx [(u'/s_L)^3 (l_t/\delta_{th})]^{1/2}$ for

Table 5.1: Initial flame and flow parameters

Φ	T_b(K)	T_u(K)	Y_{CH_4}	Y_{O_2}	Y_{CO_2}	Y_{H_2O}	s_L(m/s)	δ_{th}(mm)	Ka
1.0	2 230	300	0.055	0.220	0.137	0.120	0.507	0.36	0.94–96.7
0.9	2 140	300	0.049	0.221	0.133	0.111	0.426	0.40	1.27–81.4
0.8	2 002	300	0.044	0.223	0.122	0.099	0.329	0.46	2.01–105.2
0.7	1 844	300	0.039	0.224	0.108	0.088	0.228	0.56	3.84–159.7
0.6	1 669	300	0.034	0.225	0.093	0.076	0.136	0.78	9.84–409.2

Table 5.2: Initial turbulence parameters

cases	*1*	*2*	*3*	*4*	*5*	*6*	*7*	*8*	*9*	*10*	*11*	*12*
u' (m/s)	1.0	2.0	4.0	6.0	8.0	10.0	12.0	14.0	16.0	18.0	20.0	22.0
τ (ms)	3.20	1.60	0.80	0.53	0.40	0.32	0.27	0.23	0.20	0.18	0.16	0.15
Re_t	205	410	821	1 231	1 641	2 051	2 462	2 872	3 282	3 668	4 103	4 513

the various mixture equivalence ratios (Φ) are given in Table 5.1. The given range for the Karlovitz number Ka corresponds to the different turbulence intensities, as defined below. The initial system is a hot ($T = T_b$) perfectly spherical laminar flame-kernel of initial radius $r_o = 5.0$ mm, located at the center of the computational box and surrounded by a fresh premixed atmospheric mixture of methane and air at T_u. The initial mass fraction values of $Y_{\mathrm{CH_4}}$ and $Y_{\mathrm{O_2}}$ at T_u, and $Y_{\mathrm{CO_2}}$ and $Y_{\mathrm{H_2O}}$ at T_b are prescribed outside and within the kernel, respectively. These initial values for any primitive variable ϕ are transformed into smooth profiles according to

$$\phi = \phi_o + \frac{\Delta\phi}{2}\left\{1 - \tanh\left[s \cdot \left(\frac{r - r_o}{r_o}\right)\right]\right\} \tag{5.18}$$

where $\Delta\phi$ is the difference between the initial values (ϕ_o) in the fresh and burnt gas mixture. The integer s is a measure of the stiffness at the fresh/burnt gas interface and is in the order of a few hundred. In this range, the influence of s is confined to the very early part of the simulation and therefore does not impact the analysis presented below at later times. In all cases, an appropriate nitrogen complement is added everywhere at start.

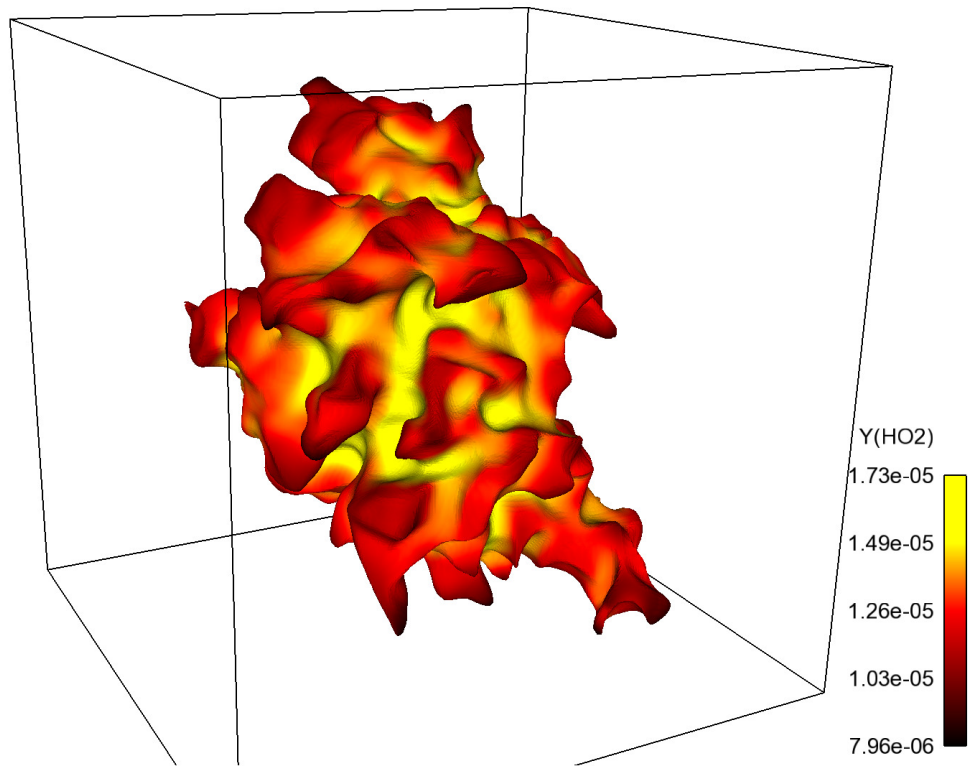

Fig. 5.1: Exemplary view of the configuration showing the heavily wrinkled iso-surface of the mass fraction of CO_2 and colored by the HO_2 flame radical

Because of the extremely high computation efforts of the three-dimensional DNS computations, the following systematic study (Section 5.4) has been realized for a two-dimensional configuration.

To investigate systematically the influence of the integral Reynolds number Re_t on the fuel consumption/burning rate, the calculations for a given Φ were repeated with exactly the same initial composition, but with an initial pseudo-turbulent velocity field at successively higher intensity. The rms velocity fluctuation u', the eddy turn-over time $\tau = l_t/u'$ and the turbulent Reynolds number Re_t for the various cases are given in Table 5.2. The characteristic kinematic viscosity of the mixture, $\nu = 1.56 \cdot 10^{-5}$ m^2/s and the integral length scale $l_t = 3.2$ mm are kept constant. Note also that not all the cases shown here are realized for every mixture composition given in Table 5.1, due to the higher sensitivity of the leaner mixtures to increasing turbulence intensity, as will be demonstrated later. For the mixtures with $\Phi = 0.6$ & 0.7, only *cases 1 – 7* are considered, while for $\Phi = 0.8$, 0.9 & 1.0, only *cases 1 – 8*, *1 – 9* and *1 – 12* are performed, respectively.

A total number of computing cores ranging between $256 - 512$ were employed to solve all the presented problems on our local Linux cluster (Kármán cluster in Magdeburg equipped with 68 dual-nodes 2.1GHz AMD Opteron quad-processors), delivering a peak performance of 5 Tflop/s. Each computation requires typically 10 days on this cluster. For all results presented below, the simulation has been carried out up to a non-dimensional time $t \geq 1.3\tau$ as recommended for DNS relying on time-decaying turbulence [70].

5.4 Computational Results

Highly turbulent conditions (Re_t up to 4 513) have been accessed for five different mixture equivalence ratios $\Phi = 0.6$, 0.7, 0.8, 0.9 and 1.0. The effect of turbulence on the physical structure of the flame is first investigated visually by examining both the instantaneous and temporal evolution of the temperature and of selected species mass fraction fields, plotted in Figs. 5.2 – 5.5.

Figs. 5.2 and 5.3 show the iso-contours of temperature (*case 8*) and mass fraction of CH_3O (*case 7*) computed with mixture equivalence ratio $\Phi = 0.8$, illustrating the physical flame structure at different non-dimensional times $t = 0.1\tau$, 0.5τ, 0.9τ and 1.3τ. Considering the temperature field, the initial laminar spherical flame (Fig. 5.2(a)) is progressively being distorted and stretched (Fig. 5.2(b)) by the very strong turbulent field with time, leading to the creation of islands (in the form of both hot and fresh gas pockets) and edge flame-like structures (Fig. 5.2(c)–5.2(d)) [11] at various locations within the computational domain and for various shapes and sizes. For a high turbulence intensity, (local) flame extinction and flame-flame interactions become important. The temporal evolution of the iso-contours of the minor radical CH_3O shown in Fig. 5.3 follow closely the patterns in the temperature field but shows much stronger and distinct discontinuities at later times ($t = 0.9$–1.3τ), illustrating high local differences in burning conditions within the same flame front. Such observations are usually not possible when looking at integrated quantities, like temperature, illustrating the importance of a more detailed description of chemical processes. Considering CH_3O, local extinction events can be determined earlier and at a finer resolution in space. Numerous fresh gas islands and flame pinch-off events are visible (Fig. 5.3(c)), evidencing local flame extinctions. Looking at the mass fraction values, the peak species mass fraction rises soon after ignition from $1.24 \cdot 10^{-5}$ at $t = 0.1\tau$ to $6.47 \cdot 10^{-5}$ at $t = 0.5\tau$, after which it drops to $5.76 \cdot 10^{-5}$ at $t = 0.9\tau$, then down to

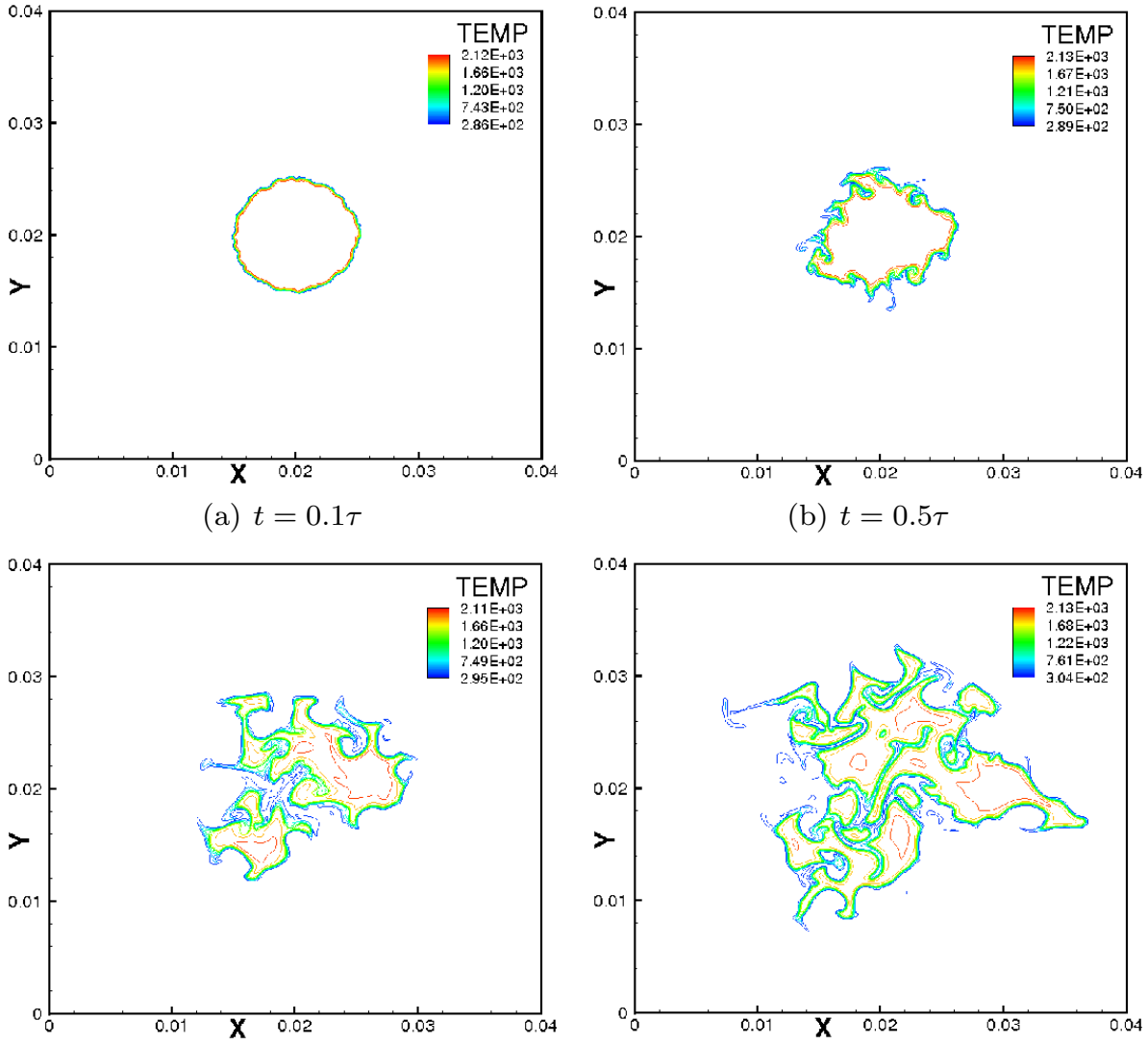

(a) $t = 0.1\tau$ (b) $t = 0.5\tau$

(c) $t = 0.9\tau$ (d) $t = 1.3\tau$

Fig. 5.2: Time evolution of the iso-contours of temperature (*case 8*, $\mathrm{Re}_t = 2\,872$) for mixture equivalence ratio $\Phi = 0.8$ at $t = 0.1\tau$, 0.5τ, 0.9τ and 1.3τ

$3.12 \cdot 10^{-5}$ at $t = 1.3\tau$. Later, complete extinction is observed for these conditions. The iso-contours of most major and minor species exhibit qualitatively similar patterns to those of the temperature and CH_3O fields, respectively.

The instantaneous flame structure is exemplified in Fig. 5.4, where the iso-surface of the mass fraction of the O radical is shown for different integral Reynolds numbers Re_t at the same non-dimensional time $t = 1.3\tau$. The fields are for the computations with $\Phi = 0.9$. Previously, DNS easily accessed mild turbulence conditions such as the one shown in Fig. 5.4(a) – 5.4(c) where

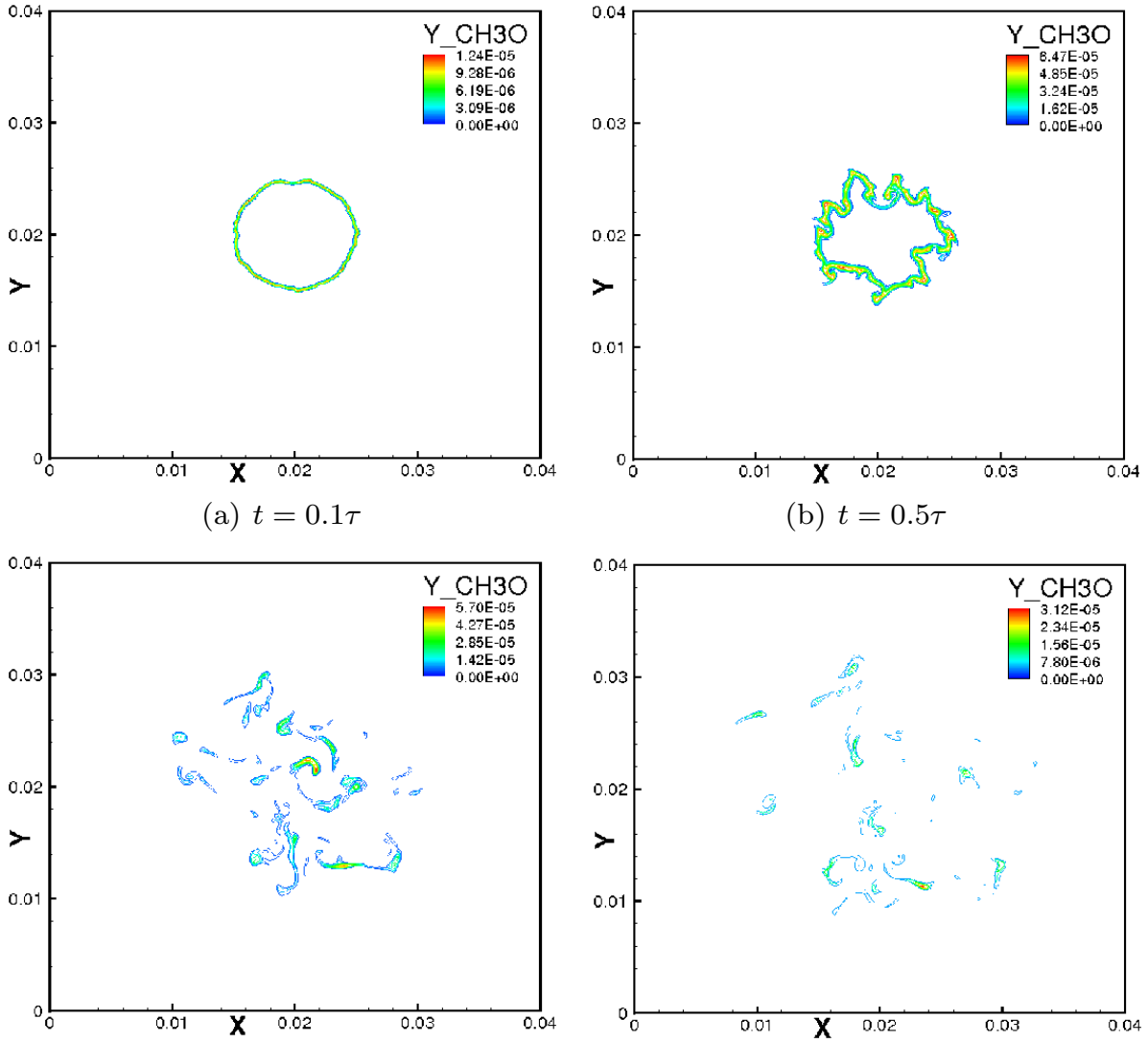

(a) $t = 0.1\tau$ (b) $t = 0.5\tau$

(c) $t = 0.9\tau$ (d) $t = 1.3\tau$

Fig. 5.3: Time evolution of the iso-contours of the mass fraction of CH_3O (*case 7*, $\mathrm{Re}_t = 2\,462$) for mixture equivalence ratio $\Phi = 0.8$ at $t = 0.1\tau$, 0.5τ, 0.9τ and 1.3τ

the flame is only slightly contorted. Comparing the snapshots in Fig. 5.4, it is observed that the amount of wrinkling increases strongly from Fig. 5.4(a) to 5.4(c) and tends to saturate afterwards (compare in particular Fig. 5.4(d) with Fig. 5.4(e)). This is an indication that Re_t should exceed noticeably 1 000 in order to reach conditions corresponding to a realistic turbulent flame, depending of course on the application. For higher values of Re_t, considerable structural modifications are observed, in particular flame–flame interactions,

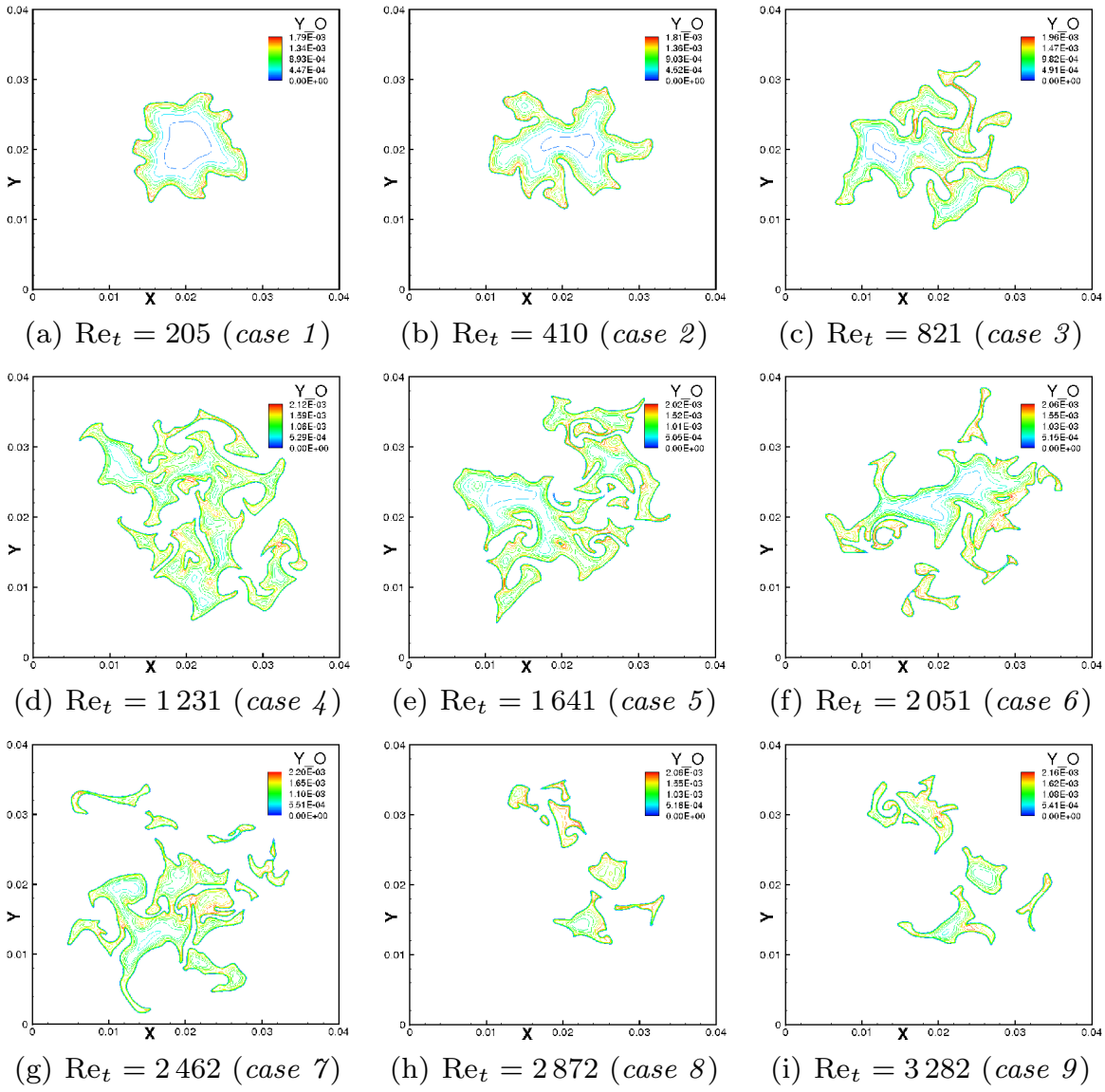

(a) $\mathrm{Re}_t = 205$ (*case 1*) (b) $\mathrm{Re}_t = 410$ (*case 2*) (c) $\mathrm{Re}_t = 821$ (*case 3*)

(d) $\mathrm{Re}_t = 1\,231$ (*case 4*) (e) $\mathrm{Re}_t = 1\,641$ (*case 5*) (f) $\mathrm{Re}_t = 2\,051$ (*case 6*)

(g) $\mathrm{Re}_t = 2\,462$ (*case 7*) (h) $\mathrm{Re}_t = 2\,872$ (*case 8*) (i) $\mathrm{Re}_t = 3\,282$ (*case 9*)

Fig. 5.4: Instantaneous iso-surface of the mass fraction of O for different integral Reynolds number Re_t at the same mixture equivalence ratio $\Phi = 0.9$ and same time $t = 1.3\tau$

leading to pinch off as evident in the higher Re_t snapshot in Fig. 5.4(c) – 5.4(e). The resulting turbulent flame structure is then marred with numerous perforations. Further increase in turbulence intensity leads to a further increase of pinch off and mutual annihilation effects, thereby limiting further increase in the flame surface area. Consequently, it drops steadily as evidenced in Fig. 5.4(f) – 5.4(i), indicating the advent of global extinction processes, as observed experimentally in combustion vessel experiments [1, 2, 3, 4].

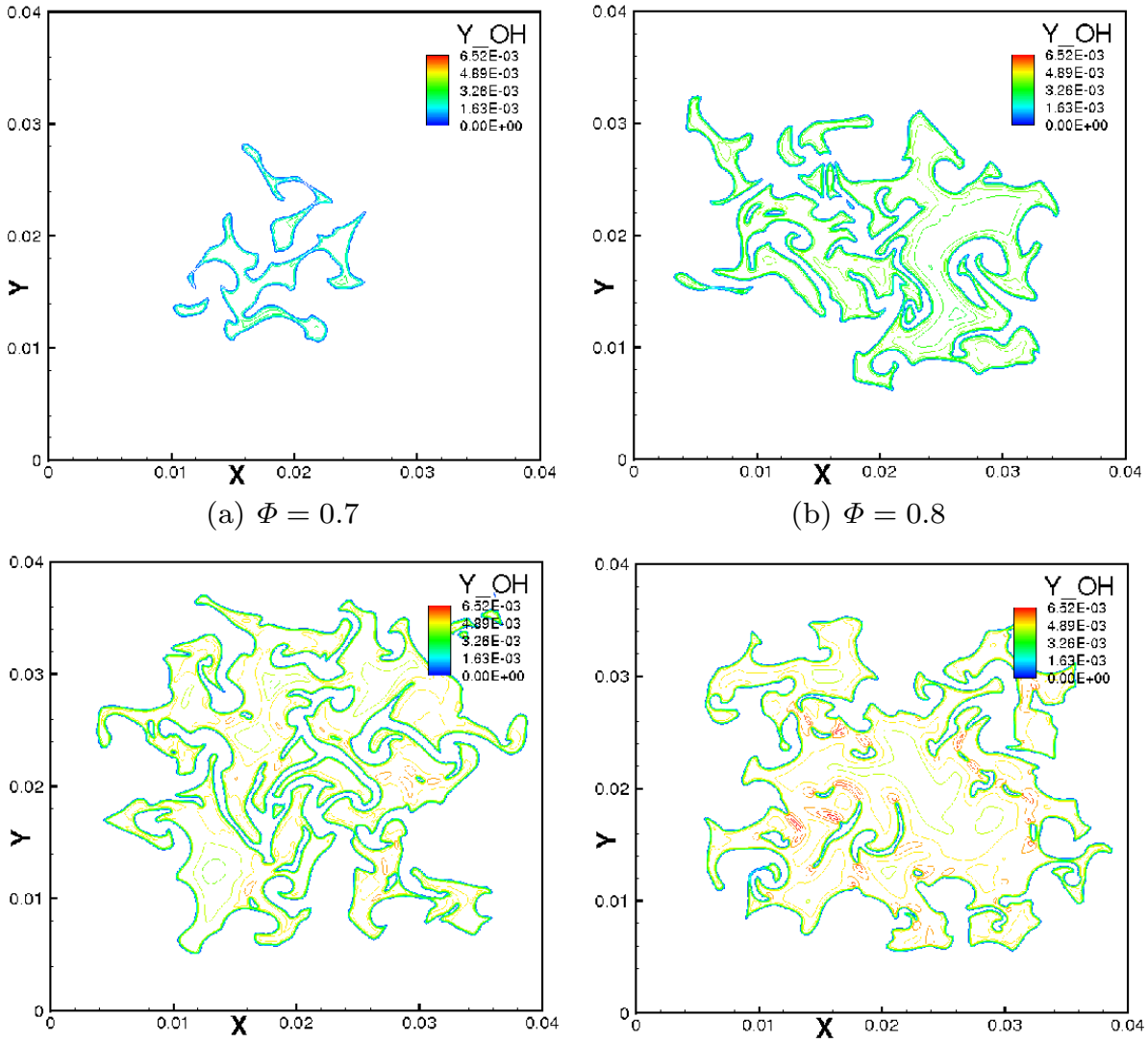

(a) $\Phi = 0.7$ (b) $\Phi = 0.8$

(c) $\Phi = 0.9$ (d) $\Phi = 1.0$

Fig. 5.5: Instantaneous iso-contours of the mass fraction of OH (*case 6*, $\mathrm{Re}_t = 2\,051$) for different mixture equivalence ratios Φ at the same time $t = 1.3\tau$

To show the effect of the equivalence ratio on the turbulent flame structure, Fig. 5.5 presents the instantaneous iso-contours of the mass fraction of OH (*case 6*) for different mixture equivalence ratios $\Phi = 0.7$, 0.8, 0.9 and 1.0 at the same time $t = 1.3\tau$. The color scale is kept identical for all plots. The lower flame activity when decreasing the equivalence ratio can easily be seen on this figure, explaining again why global flame extinction is systematically observed earlier at lower values of Φ. Since the employed chemical scheme has

only been validated for lean to stoichiometric conditions, similar studies for rich conditions cannot be presented yet.

5.5 Conclusion

A huge three-dimensional Direct Numerical Simulation (DNS) as well as a two-dimensional systematic study of turbulent flames at realistic (i.e., high) values of the Reynolds number based on the integral scale have been realized. All the computations employ the reactive Navier-Stokes equations including accurate models for chemistry and molecular transport. For these investigations the ignition and propagation of turbulent methane flames, modeled using up to 16 chemical species, were considered. Very high turbulent Reynolds number were simulated for typical flame configurations, revealing significant structural modifications of the turbulent flame shape.

The massively parallel three-dimensional DNS flame solver, *Parcomb3D* was upgraded, optimized and used extensively in a previous project. The total number of 1 558 072 *CPU-hours*, which were initially allocated for that project (Direct Numerical Simulations of Turbulent Flames at High Reynolds Numbers, Project acronym: DNS-HiRe) on three different High Performance Computing (HPC) systems:

- IBM Power5 Cluster (HPCx) at EPCC (Scotland),
- CRAY (HECToR X2) at EPCC (Scotland),
- BlueGene/P (BABEL) at IDRIS (France)

within the DEISA (Distributed European Infrastructure for Supercomputing Applications under the auspices of the 7^{th} Framework program financed by the European Union) network across Europe were completely expended. Both premixed and non-premixed flame configurations were considered for various fuels.

Thanks to DEISA, it has been possible to access the largest existing supercomputers in Europe, allowing DNS computations at high Reynolds numbers while taking into account chemical processes in a realistic manner.

Chapter 6

Summary

6.1 New Scientific Results

I. The spectral entropy is introduced based on proper orthogonal decomposition (POD). It is a convenient property to uniquely quantify the flow state and differentiate between laminar, transitional, or turbulent regime.
The dimensionless spectral entropy is defined from the eigenvalues obtained by solving the eigenvalue problem for the temporal autocorrelation function. It is zero for a steady state problem, otherwise positive. Our previous systematic study showed that a fully developed turbulent flow can be characterized by values larger than $0.7 - 1.1$ [6].

II. Well-resolved large eddy simulation (LES) is presented in a pipe with sudden expansion. The results show exceptionally good agreement compared with experimental data. The engineering turbulence model are not able to predict the laminar, transitional and turbulent regimes simultaneously [42]. (Chapter 3)

III. The spectral entropy can characterize well different flow regimes, such as laminar, transitional or turbulent flows. It is demonstrated that this quantity can be applied for hybrid simulations [17], where only the turbulent regimes are well-resolved thus reducing the overall computational costs. (Chapter 3)

IV. The three-dimensional turbulent flow is studied in a stirred tank reactor using POD analysis to determine the coherent flow structures, e.g., the secondary flow structures [43]. (Chapter 4)

V. The macro-instabilities (MI) are investigated by the FFT analysis of the temporal coefficients obtained from the POD analysis. These low frequency flow oscillations for the present configuration correspond to around one-eighth and one-fifth of the blade passage frequency (BPF). The MIs influence in particular the mixing efficiency in a stirred tank, proving the applicability of the presented methods for the further optimization of such a system [43]. (Chapter 4)

VI. Turbulent flows with chemical reactions are studied using direct numerical simulations (DNS). The Navier-Stokes equations for compressible flows are extended by detailed chemical and transport models involving many individual species. A spatial sixth-order central stencil, progressively reduced to a one-sided fourth-order scheme near the boundaries is used for spatial discretization. Time integration is performed in an explicit manner with a fourth-order Runge-Kutta scheme [5] [27] [28] [29].

VII. The simulation is parallelized using a three-dimensional domain decomposition and MPI communication library. The combustion process of the methane gas is described using 16 chemical species and 50 elementary reactions. Therefore, 16 transport equations are solved additionally to the flow governing equations. The presented results for various Reynolds numbers represent the state-of-the art considering combustion processes computed by DNS simulations [27] [28] [29]. (Chapter 5)

VIII. The DNS code employed in this work is a massively parallel flame solver, which solves the full compressible reactive Navier-Stokes system coupled with detailed chemistry and multicomponent transport models. The high-fidelity computations can provide detailed understanding for the interaction between the fluid dynamics and chemical processes. A systematic study varying the Reynolds number is performed to study the effect of turbulence on the combustion process. The extinction probability of the flame increases with the turbulence intensity [27] [28] [29]. (Chapter 5)

6.2 Conclusions

The numerical simulations of complex turbulent flows involving complex chemical processes have been demonstrated in this thesis, providing very efficient numerical methods for the CFD procedure. Various applications have been shown for different problems occurring in engineering.

The benchmark nozzle with a sudden expansion initially proposed by the FDA was investigated in the first application example (Chapter 3). The LES

dc_1631_19

computational results showed excellent agreement compared with PIV measurements. The different flow regimes were characterized by the spectral entropy.

Next, the turbulent flow in a stirred tank was analyzed using LES simulations in Chapter 4. The coherent flow structures of the complex three-dimensional turbulent hydrodynamics were successfully extracted using the 3D Snapshot POD method. The macro-instability was studied because it is believed that it plays a crucial role concerning mixing, hence product quality.

Using powerful parallel supercomputers, accurate physical models and efficient numerical techniques, complex three-dimensional turbulent flames can be computed as "numerical experiments" using Direct Numerical Simulation as considered in Chapter 5. Interesting information can be obtained in this way concerning, e.g., the modifications of the local flame structure induced by the turbulence, or concerning flame acoustics.

As a whole, this work has shown that numerical simulation is now a mature tool for complex turbulent flow problems.

dc_1631_19

References

1. Abdel-Gayed, R., Al-khishali, K., Bradley, D.: Turbulent burning velocities and flame straining in explosions. Proceedings of the Royal Society of London. Series A, Mathematical and Physical Sciences **A391**, 393–414 (1984)
2. Abdel-Gayed, R., Bradley, D.: A two-eddy theory of premixed turbulent flame propagation. Philosophical Transactions of the Royal Society of London. Series A, Mathematical and Physical Sciences **1**(A301), 1–25 (1981)
3. Abdel-Gayed, R., Bradley, D.: The influence of turbulence upon the rate of burning. In: J. Lee, C. Guirao, D. Grierson (eds.) Proceedings of the international conference on fuel-air explosions, no. 16 in Studies series, pp. 51–68. University of Waterloo Press, McGill University (1982)
4. Abdel-Gayed, R., Bradley, D., Lawes, M.: Turbulent burning velocities: A general correlation in terms of straining rates. Proceedings of the Royal Society of London. Series A, Mathematical and Physical Sciences **A414**, 389–413 (1987)
5. Abdelsamie, A., Fru, G., Oster, T., Dietzsch, F., Janiga, G., Thévenin, D.: Towards direct numerical simulations of low-Mach number turbulent reacting and two-phase flows using immersed boundaries. Computers & Fluids **131**, 123–141 (2016)
6. Abdelsamie, A., Janiga, G., Thévenin, D.: Spectral entropy as a flow state indicator. International Journal of Heat and Fluid Flow **68**, 102–113 (2017)
7. Anderson, J.: Computational fluid dynamics: The basics with applications. McGraw-Hill, New York (1995)
8. ANSYS Inc.: ANSYS FLUENT Theory Guide Release 14.0. Canonsburg, PA (2011)
9. Arányi, P., Janiga, G., Zähringer, K., Thévenin, D.: Analysis of different POD methods for PIV-measurements in complex unsteady flows. International Journal of Heat and Fluid Flow **43**, 204–211 (2013)
10. Baum, M., Poinsot, T., Thévenin, D.: Accurate boundary conditions for multicomponent reactive flows. Journal of Computational Physics **116**, 247–261 (1995)
11. Bédat, B., Egolfopoulos, F., Poinsot, T.: Direct numerical simulation of heat release and nox formation in turbulent non premixed flames. Combustion and Flame **119**, 69–83 (1999)

12. Bilger, R., Esler, M., Stårner, S.: On reduced mechanisms for methane-air combustion. In: M.D. Smooke (ed.) Reduced Kinetic Mechanisms and Asymptotic Approximations for Methane-Air Flames, *Lecture Notes in Physics*, vol. 384, pp. 86–110. Springer-Verlag (1991)
13. Bowman, C., Hanson, R., Gardiner, W., Lissiansk, V., Frenklach, M., Goldenberg, M., Smith, G., Crosley, D., Golden, D.: An optimized detailed chemistry reaction mechanism for methane combustion and no formation and reburning. Tech. Rep. GRI-97/0020, Gas research Institute, Chicago, IL (1997)
14. Byrne, G., Mut, F., Cebral, J.: Quantifying the large-scale hemodynamics of intracranial aneurysms. American Journal of Neuroradiology **35**, 333–338 (2014)
15. Cant, S.: Direct numerical simulation of premixed turbulent flames. Philosophical Transactions of the Royal Society A **357**(1764), 3583–3604 (1999)
16. Cifuentes, L., Dopazo, C., Martín, J., Domingo, P., Vervisch, L.: Local volumetric dilatation rate and scalar geometries in a premixed methane–air turbulent jet flame. Proceedings of the Combustion Institute **35**, 1295–1303 (2015)
17. Daróczy, L., Abdelsamie, A., Janiga, G., Thévenin, D.: State detection and hybrid simulation of biomedical flows. In: 10th International Symposium on Turbulence and Shear Flow Phenomena, pp. 280/1–6 (2017)
18. Davidson, L., Dahlström, S.: Hybrid RANS-LES: An approach to make LES applicable at high Reynolds number. Int. J. Comput. Fluid Dyn. **19**(6), 415–427 (2005)
19. Delafosse, A., Line, A., Morchain, J., Guiraud, P.: LES and URANS simulations of hydrodynamics in mixing tank: Comparison to PIV experiments. Chemical Engineering Research and Design **86**(12), 1322–1330 (2008)
20. Delorme, Y., Anupindi, K., Frankel, S.: Large eddy simulation of FDA's idealized medical device. Cardiovascular Engineering and Technology **4**(4), 392–407 (2013)
21. Domingo, P., Vervisch, L., Réveillon, J.: Dns analysis of partially premixed combustion in spray and gaseous turbulent flame-bases stabilized in hot air. Combustion and Flame **140**(3), 172–195 (2005)
22. Doulgerakis, Z., Yianneskis, M., Ducci, A.: On the manifestation and nature of macroinstabilities in stirred vessels. AIChE Journal **57**(11), 2941–2954 (2011)
23. Eng, M., Rasmuson, A.: Large eddy simulation of the influence of solids on macro instability frequency in a stirred tank. Chemical Engineering Journal **259**, 900–910 (2015)
24. Ferziger, J.H., Perić, M.: Computational Methods for Fluid Dynamics. Springer-Verlag, Berlin, Heidelberg (1999)
25. Fru, G., Janiga, G., Thévenin, D.: Direct numerical simulation of turbulent methane flames with and without volume viscosity. In: 8th Euromech Fluid Mechanics Conference (EFMC-8), pp. MS2–9. Bad Reichenhall, Germany (2010)
26. Fru, G., Janiga, G., Thévenin, D.: Direct numerical simulation of highly turbulent premixed flames burning methane. In: H. Kuerten, B. Geurts, V. Armenio, J. Fröhlich (eds.) Direct and Large-Eddy Simulation VIII, ERCOFTAC Series, pp. 327–332. Springer-Verlag, Eindhoven (2011)
27. Fru, G., Janiga, G., Thévenin, D.: Direct numerical simulations of the impact of high turbulence intensities and volume viscosity on premixed methane flames. Journal of Combustion **2011**, 746 719/1–12 (2011)
28. Fru, G., Janiga, G., Thévenin, D.: Impact of volume viscosity on the structure of turbulent premixed flames in the thin reaction zone regime. Flow, Turbulence and Combustion **88**, 451–478 (2012)

29. Fru, G., Thévenin, D., Janiga, G.: Impact of turbulence intensity and equivalence ratio on the burning rate of premixed methane-air flames. Energies **4**(6), 878–893 (2011)
30. Geurts, B.: Elements of direct and large-eddy simulation. R. T. Edwards Incorporated, Philadelphia, PA (2004)
31. Hariharan, P., Giarra, M., Reddy, V., Day, S.W., Manning, K.B., Deutsch, S., Stewart, S.F.C., Myers, M.R., Berman, M.R., Burgreen, G.W., Paterson, E.G., Malinauskas, R.A.: Multilaboratory particle image velocimetry analysis of the FDA benchmark nozzle model to support validation of computational fluid dynamics simulations. Journal of Biomechanical Engineering **133**, 041 002/1–14 (2011)
32. Hartmann, H., Derksen, J.J., Montavon, C., Pearson, J., Hamill, I.S., van den Akker, H.E.A.: Assessment of large eddy and RANS stirred tank simulations by means of LDA. Chemical Engineering Science **59**(12), 2419–2432 (2004)
33. Hasal, P., Jahoda, M., Fořt, I.: Macro-instability: A chaotic flow component in stirred tanks. Philosophical Transactions of the Royal Society A: Mathematical, Physical and Engineering Sciences **366**(1864), 409–418 (2008)
34. Hasal, P., Montes, J.L., Boisson, H.C., Fořt, I.: Macro-instabilities of velocity field in stirred vessel: Detection and analysis. Chemical Engineering Science **55**(2), 391–401 (2000)
35. Hawkes, E., Sankaran, R., Sutherland, J., Chen, J.H.: Scalar mixing in direct numerical simulations of temporally evolving plane jet flames with skeletal CO/H_2 kinetics. Proceedings of the Combustion Institute **31**(1), 1633–1640 (2007)
36. Hilbert, R., Tap, F., El-Rabii, H., Thévenin, D.: Impact of detailed chemistry and transport models on turbulent flame simulations. Progress in Energy and Combustion Science **30**(1), 61–117 (2004)
37. Hilbert, R., Thévenin, D.: Influence of differential diffusion on maximum flame temperature in turbulent nonpremixed hydrogen/air flames. Combustion and Flame **138**(1-2), 175–187 (2004)
38. Hinze, J.O.: Turbulence. McGraw-Hill, New York (1975)
39. Holmes, P.J., Lumley, J.L., Berkooz, G., Mattingly, J.C., Wittenberg, R.W.: Low-dimensional models of coherent structures in turbulence. Physics Reports **287**(4), 337–384 (1997)
40. Honein, A., Moin, P.: Higher entropy conservation and numerical stability of compressible turbulence simulations. Journal of Computational Physics **201**(2), 531–545 (2004)
41. James, S., Jaberi, F.: Large scale simulations of two-dimensional nonpremixed methane jet flames. Combustion and Flame **123**, 465–487 (2000)
42. Janiga, G.: Large eddy simulation of the FDA benchmark nozzle for a Reynolds number of 6500. Computers in Biology and Medicine **47**, 113–119 (2014)
43. Janiga, G.: Large-eddy simulation and 3D proper orthogonal decomposition of the hydrodynamics in a stirred tank. Chemical Engineering Science **201**, 132–144 (2019)
44. Janiga, G.: Novel feature-based visualization of the unsteady blood flow in intracranial aneurysms with the help of proper orthogonal decomposition (POD). Computerized Medical Imaging and Graphics **73**, 30–38 (2019)
45. Janiga, G.: Quantitative assessment of 4D hemodynamics in cerebral aneurysms using proper orthogonal decomposition. Journal of Biomechanics **82**, 80–86 (2019)

46. Janiga, G., Stucht, D., Bordás, R., Temmel, E., Seidel-Morgenstern, A., Thévenin, D., Speck, O.: Noninvasive 4D flow characterization in a stirred tank via phase-contrast magnetic resonance imaging. Chemical Engineering and Technology **40**(7), 1370–1327 (2017)
47. Jeong, J., Hussain, F.: On the identification of a vortex. Journal of Fluid Mechanics **285**, 69–94 (1995)
48. Joshi, J.B., Nere, N.K., Rane, C.V., Murthy, B.N., Mathpati, C.S., Patwardhan, A.W., Ranade, V.V.: CFD simulation of stirred tanks: Comparison of turbulence models. Part I: Radial flow impellers. Canadian Journal of Chemical Engineering **89**(1), 23–82 (2011)
49. Joshi, J.B., Nere, N.K., Rane, C.V., Murthy, B.N., Mathpati, C.S., Patwardhan, A.W., Ranade, V.V.: CFD simulation of stirred tanks: Comparison of turbulence models. Part II: Axial flow impellers, multiple impellers and multiphase dispersions. Canadian Journal of Chemical Engineering **89**(4), 754–816 (2011)
50. Kallmes, D.F.: Point: CFD–computational fluid dynamics or confounding factor dissemination. American Journal of Neuroradiology **33**(3), 395–396 (2012)
51. Kolmogorov, A.N.: Local structure of turbulence in incompressible viscous fluid for very large Reynolds number. Doklady Akademija Nauk, SSSR **30**, 299–303 (1941)
52. Laverdant, A.: Notice d'utilisation du programme SIDER (PARCOMB3D). Tech. Rep. RTS 3/12488 DEFA, The French Aerospace Lab., ONERA (2008)
53. Lele, S.K.: Compact finite difference schemes with spectral-like resolution. Journal of Computational Physics **103**(1), 16–42 (1992)
54. Lilly, D.K.: A proposed modification of the Germano sugrid-scale closure method. Physics of Fluids A **4**(3), 633–635 (1992)
55. Liné, A., Gabelle, J.C., Morchain, J., Anne-Archard, D., Augier, F.: On pod analysis of piv measurements applied to mixing in a stirred vessel with a shear thinning fluid. Chemical Engineering Research and Design **91**(11), 2073–2083 (2013)
56. Löhner, R.: Applied computational fluid dynamics techniques: an introduction based on finite element methods. Wiley, Chichester (2008)
57. Lu, P.C., Gross, D.R., Hwang, N.H.C.: Intravascular pressure and velocity fluctuations in pulmonic arterial stenosis. Journal of Biomechanics **13**(3), 291–300 (1980)
58. Lumley, J.L.: Coherent structures in turbulence. In: Transition and Turbulence, pp. 215–242. Academic Press (1981)
59. Moin, P.: Advances in large eddy simulation methodology for complex flows. International Journal of Heat and Fluid Flow **23**(5), 710–720 (2002)
60. Molla, M.M., Wang, B.C., Kuhn, D.C.S.: Numerical study of pulsatile channel flows undergoing transition triggered by a modelled stenosis. Physics of Fluids **24**, 121 901/1–25 (2012)
61. Murthy, B.N., Joshi, J.B.: Assessment of standard $k-\epsilon$, RSM and LES turbulence models in a baffled stirred vessel agitated by various impeller designs. Chemical Engineering Science **63**(22), 5468–5495 (2008)
62. Nikiforaki, L., Montante, G., Lee, K.C., Yianneskis, M.: On the origin, frequency and magnitude of macro-instabilities of the flows in stirred vessels. Chemical Engineering Science **58**, 2937–2949 (2003)
63. Patankar, S.: Numerical heat transfer and fluid flow. Hemisphere Publishing Corporation (1980)

64. Poinsot, T.: Using direct numerical simulations to understand premixed turbulent combustion. Proceedings of the Combustion Institute **26**, 219–232 (1992)
65. Poinsot, T.J., Lele, S.K.: Boundary conditions for direct simulations of compressible viscous flows. Journal of Computational Physics **101**(1), 104–129 (1992)
66. Pope, S.B.: Turbulent flows. Cambridge University Press, Cambridge (2000)
67. Revstedt, J., Fuchs, L., Trägårdh, C.: Large eddy simulations of the turbulent flow in a stirred reactor. Chemical Engineering Science **53**(24), 4041–4053 (1998)
68. Roberts, W., Driscoll, J., Drake, M., Goss, L.: Images of the quenching of a flame by a vortex – to quantify regimes of turbulent combustion. Combustion and Flame **94**, 58 (1993)
69. Roussinova, V., Kresta, S.M., Weetman, R.: Low frequency macroinstabilities in a stirred tank: scale-up and prediction based on large eddy simulations. Chemical Engineering Science **58**(11), 2297–2311 (2003)
70. Rutland, C.J., Ferziger, J., El Thary, S.: Full numerical simulations and modeling of turbulent premixed flames. Proceedings of the Combustion Institute **23**, 621–627 (1990)
71. Sagaut, P.: Large eddy simulation for incompressible flows: An introduction. Springer, Berlin, Heidelberg, New York (2006)
72. Sagaut, P., Deck, S., Terracol, M.: Multiscale and multiresolution approaches in turbulence, LES, DES and hybrid RANS/LES methods: applications and guidelines, 2nd edn. Imperial College Press, London (2013)
73. Sirovich, L.: Turbulence and the dynamics of coherent structures: I, coherent structures; II, symmetry and transformations; III, dynamics and scaling. Quart Appl Mathematics **45**(3), 561–590 (1987)
74. Smagorinsky, J.: General circulation experiments with the primitive equations, part I: The basic experiment. Monthly Weather Review **91**, 99–164 (1963)
75. Smooke, M.D., Giovangigli, V.: Formulation of the premixed and nonpremixed test problems. In: M.D. Smooke (ed.) Reduced Kinetic mechanism and Asymptotic Approximations for Methane-Air Flames, *Lecture Notes in Physics*, vol. 384, pp. 1–28. Springer-Verlag (1991)
76. Sommerfeld, M., Decker, S.: State of the art and future trends in CFD simulation of stirred vessel hydrodynamics. Chemical Engineering and Technology **27**(3), 215–224 (2004)
77. Sotiropoulos, F.: Computational fluid dynamics for medical device design and evaluation: Are we there yet? Cardiovascular Engineering and Technology **3**(2), 137–138 (2012)
78. de Souza, L.M., Janiga, G., Thévenin, D.: Multi-objective optimisation of the model parameters for the realisable $k - \varepsilon$ turbulence model. Progress in Computational Fluid Dynamics **17**(2), 90–101 (2017)
79. Stewart, S.F.C., Paterson, E.G., Burgreen, G.W., Hariharan, P., Giarra, M., Reddy, V., Day, S.W., Manning, K.B., Deutsch, S., Berman, M.R., Myers, M.R., Malinauskas, R.A.: Assessment of CFD performance in simulations of an idealized medical device: Results of FDA's first computational interlaboratory study. Cardiovascular Engineering and Technology **3**(2), 139–160 (2012)
80. Tabib, M.V., Joshi, J.B.: Analysis of dominant flow structures and their flow dynamics in chemical process equipment using snapshot proper orthogonal decomposition technique. Chemical Engineering Science **63**(14), 3695–3715 (2008)

81. Thévenin, D., Behrendt, F., Maas, U., Przywara, B., Warnatz, J.: Development of a parallel direct simulation code to investigate reactive flows. Computers & Fluids **25**(5), 485–496 (1996)
82. Versteeg, H., Malalasekera, W.: An introduction to computational fluid dynamics: The finite volume method. Addison-Wesley (1996)
83. Warnatz, J., Maas, U., Dibble, R.W.: Combustion, 3rd edn. Springer (2001)
84. Wilcox, D.C.: Turbulence modeling for CFD. DCW Industries, Inc., La Cañada, California (1998)
85. Yeoh, S.L., Papadakis, G., Yianneskis, M.: Numerical simulation of turbulent flow characteristics in a stirred vessel using the LES and RANS approaches with the sliding/deforming mesh methodology. Chemical Engineering Research and Design **82**(7), 834–848 (2004)
86. Zhao, Q., Zhang, T., Liu, Y., Cao, X., Wang, S., Zhao, H.: Comparative study of RANS and LES simulation methods for analysis of turbulence in a tubular stirred reactor. Advanced Materials Research **499**, 218–222 (2012)
87. Zmijanovic, V., Mendez, S., Moureau, V., Nicoud, F.: About the numerical robustness of biomedical benchmark cases: Interlaboratory FDA's idealized medical device. International Journal for Numerical Methods in Biomedical Engineering **33**(1), e02 789 (2017)

Appendix A

Chemical Mechanism of Smooke

The methane oxidation in Chapter 5 is modeled by a 25-step skeletal scheme [12, 75], comprised of 4 elements (H, C, O, N), 16 chemical species (CH_4, O_2, H_2, H_2O, CH_2O, CO, CO_2, HO_2, OH, H, O, CH_3, HCO, H_2O_2, CH_3O, N_2) and 50 elementary reactions.

Table A.1: Skeletal Mechanism of Smooke

#							A_i (cgs)	β_i	E_i (cgs)
1	H	+ O_2		= OH	+ O		2.000×10^{14}	0.0	16800.0
2	O	+ H_2		= OH	+ H		1.800×10^{10}	1.0	8826.0
3	H_2	+ OH		= H_2O	+ H		1.170×10^{09}	1.3	3626.0
4	OH	+ OH		= O	+ H_2O		6.000×10^{08}	1.3	00.0
5	H	+ O_2	+ M	= HO_2	+ M		2.300×10^{18}	-0.8	00.0
6	H	+ HO_2		= OH	+ OH		1.500×10^{14}	0.0	1004.0
7	H	+ HO_2		= H_2	+ O_2		2.500×10^{13}	0.0	0700.0
8	OH	+ HO_2		= H_2O	+ O_2		2.000×10^{13}	0.0	1000.0
9	CO	+ OH		= CO_2	+ H		1.510×10^{07}	1.3	-0758.0
10	CH_4	+ M		= CH_3	+ H	+ M	2.300×10^{38}	-7.0	114360.0
11	CH_4	+ H		= CH_3	+ H_2		2.200×10^{04}	3.0	8750.0
12	CH_4	+ OH		= CH_3	+ H_2O		1.600×10^{06}	2.1	2460.0
13	CH_3	+ O		= CH_2O	+ H		6.800×10^{13}	0.0	00.0
14	CH_2O	+ H		= HCO	+ H_2		2.500×10^{13}	0.0	3991.0
15	CH_2O	+ OH		= HCO	+ H_2O		3.000×10^{13}	0.0	1195.0
16	HCO	+ H		= CO	+ H_2		4.000×10^{13}	0.0	00.0
17	HCO	+ M		= CO	+ H	+ M	1.600×10^{14}	0.0	14700.0
18	CH_3	+ O_2		= CH_3O	+ O		7.000×10^{12}	0.0	25652.0
19	CH_3O	+ H		= CH_2O	+ H_2		2.000×10^{13}	0.0	00.0
20	CH_3O	+ M		= CH_2O	+ H	+ M	2.400×10^{13}	0.0	28812.0
21	HO_2	+ HO_2		= H_2O_2	+ O_2		2.000×10^{12}	0.0	00.0
22	H_2O_2	+ M		= OH	+ OH	+ M	1.300×10^{17}	0.0	45500.0
23	H_2O_2	+ OH		= H_2O	+ HO_2		1.000×10^{13}	0.0	1800.0
24	OH	+ H	+ M	= H_2O	+ M		2.200×10^{22}	-2.0	00.0

Table A.1: Skeletal Mechanism of Smooke (cont.)

#						A_i (cgs)	β_i	E_i (cgs)
25	H	+ H	+ M	= H_2	+ M	1.800×10^{18}	-1.0	00.0

dc_1631_19